Simultaneous physical retrieval of surface emissivity spectrum and atmospheric parameters from infrared atmospheric sounder interferometer spectral radiances

Guido Masiello and Carmine Serio*

CNISM, Unità di Ricerca Università della Basilicata, Via Ateneo Lucano 10, Potenza 85100, Italy

*Corresponding author: carmine.serio@unibas.it

The problem of simultaneous physical retrieval of surface emissivity, skin temperature, and temperature, water–vapor, and ozone atmospheric profiles from high-spectral-resolution observations in the infrared is formulated according to an inverse problem with multiple regularization parameters. A methodology has been set up, which seeks an effective solution to the inverse problem in a generalized L-curve criterion framework. The *a priori* information for the surface emissivity is obtained on the basis of laboratory data alone, and that for the atmospheric parameters by climatology or weather forecasts. To ensure that we deal with a problem of fewer unknowns than observations, the dimensionality of the emissivity is reduced through expansion in Fourier series. The main objective of this study is to demonstrate the simultaneous retrieval of emissivity, skin temperature, and atmospheric parameters with a two-dimensional L-curve criterion. The procedure has been demonstrated with spectra observed from the infrared atmospheric sounder interferometer, flying onboard the *European Meteorological Operational* satellite. To check the quality and reliability of the methodology, we have used spectra recorded over regions characterized by known or stable emissivity. These include sea surface, for which effective emissivity models are known, and arid lands (Sahara and Namib Deserts) that are known to exhibit the characteristic spectral signature of quartz-rich sand. © 2013 Optical Society of America

OCIS codes: (010.0010) Atmospheric and oceanic optics; (010.0280) Remote sensing and sensors; (010.1280) Atmospheric composition; (280.4991) Passive remote sensing.

http://dx.doi.org/10.1364/AO.52.002428

1. Introduction

In general, the problem of retrieving surface emissivity from infrared spectral observations is mainly that of separating surface temperature from emissivity in the surface radiation emission. This problem is commonly referred to as $T_s − \varepsilon$ (temperature–emissivity) separation (e.g., [1–6]). Within the framework of high-spectral-resolution infrared observations from airplanes and satellites, the problem has been addressed by Knuteson and co-workers [7,8], who arrived at a closed form in which emissivity is separated from surface temperature and atmospheric emission. Thus, emissivity could be retrieved, assuming that the state of the atmosphere along with the surface temperature were known. Under suitable assumptions for the dependence of the emissivity with wavenumber, this scheme can also be used to develop a least-squares procedure in which T_s and ε are simultaneously retrieved.

Similar approaches have been considered in many studies aimed at estimating surface emissivity from aircraft, ship, and *in situ* observations of spectral radiance, normally acquired with Fourier transform

spectrometers [9–13]. These methods assume that the atmospheric state vector is known from independent sources, whereas the methodology we describe and demonstrate retrieves surface and atmospheric parameters simultaneously from spectral information contained in the Earth emission spectrum.

Several algorithms have been developed to derive emissivity in the infrared from satellite measurements [14–23]. The retrieval is normally accomplished with multistage algorithms that separate temperature and emissivity using, in addition, background emissivity information derived from laboratory measurements.

One issue of emissivity retrieval is the fact that the emissivity parameters potentially have a dimensionality as large as that of the observed radiance vector. For a given spectral observation, this could lead to an inverse problem with more unknowns than data points. Thus, the problem of effectively retrieving emissivity from infrared observations is fundamentally one of emissivity-dimension reduction, to which one possible solution was recently given in [24–26], through decomposition of the emissivity function in a suitable orthogonal basis. However, the orthogonal-basis technique dates back to [27].

It should be stressed that the emissivity seen from a satellite is dependent on the geometry of the scene as imaged by the instrument optics. The scene can contain different elements, such as soil, bedrock, and vegetation. In addition, vegetation may be in different phenological states (dry, senescent, green) and the surface influenced from seasonal snow cover. Thus, what we retrieve from the satellite observations is an *equivalent* emissivity, which only in the case of homogenous and flat surfaces (e.g., sea or desert sand) retains most of the characteristics of the emissivity spectrum measured in the laboratory.

Our objective is to devise a method to retrieve the emissivity spectrum along with atmospheric parameters, considering that in most cases our *a priori* information for emissivity could be a loose constraint. Toward this objective, we should consider that any nadir-looking instrument, such as IASI (the Infrared Atmospheric Sounding Interferometer; see [28]), yields observations that are strongly affected by surface emissivity.

The most powerful and natural way we have to represent a spectrum is its decomposition in Fourier harmonics or coefficients. This is the approach we take in this study. The emissivity spectrum is decomposed in a Fourier cosine series, and the coefficients of the expansion are retrieved instead of the spectral ordinates themselves. This allows us to represent the emissivity spectrum with the spectral resolution needed for the kind of surface at hand. This method was introduced in [29] and is here combined with a novel methodology that allows us to optimize the retrieval of emissivity independently of that for the atmospheric parameters. In fact, we develop a full two-dimensional (2D) L-curve criterion [30] for the determination of suitable regularization parameters,

which is particularly suited for the case at hand, in which the desired solution exhibits at least two distinct features simultaneously, one related to the surface emission and the second to the atmospheric emission.

It is important to stress that while our methodology uses an orthogonal basis, and in this respect shares commonality with [24–26], it does exploit a novel inverse approach, which, as stated above, makes use of a full 2D L-curve criterion [30]. To our knowledge, this aspect is original and this is the first time it has been used to retrieve surface emissivity and atmospheric parameters from high-spectral-resolution infrared observations.

The present study is mostly intended to show that the concept of simultaneous retrieval of emissivity, skin temperature, and atmospheric parameters through optimal estimation combined with a 2D L-curve criterion is feasible. The methodology is demonstrated and exemplified with the use of IASI data recorded over different types of surface. These include sea surface, desert sand, and dune fields, for which emissivity can be considered stable throughout the year and well characterized by spectral fingerprints, which can be exploited to check the quality and reliability of the retrieval methodology.

The paper is organized as follows: Section 2 shows the mathematical details of the forward/inverse formulation of the retrieval problem. Application to IASI data is shown in Section 3. Conclusions are reported in Section 4.

2. Mathematical Background: Formulation of the Forward/Inverse Problem

The methodology we present in this section is quite general and can be applied to any spectrometer of the same class as the atmospheric infrared sounder (AIRS) or IASI. However, to streamline the derivation of the methodology we will consider the case of the IASI instrument.

IASI was developed in France by the Centre National d'Etudes Spatiales (CNES) and is flying onboard the *MetOp-A* (*Meteorological Operational Satellite*) platform, the first of three satellites of the European Organization for the Exploitation of Meteorological Satellites (EUMETSAT) European Polar System. IASI has primarily been put in orbit to work for a meteorological mission, and hence its main objective is to provide suitable information on temperature and water–vapor profiles. The instrument has spectral coverage extending from 645 to 2760 cm^{-1}, which with a sampling interval $\Delta\sigma = 0.25$ cm^{-1} gives 8461 data points or channels for each single spectrum. Data samples are taken at intervals of 25 km along and across track, each sample having a minimum diameter of about 12 km. With a swath width on Earth's surface of about 2000 km, global coverage is achieved in 12 h, during which the instrument records about 650,000 spectra. Further details on IASI and its mission objectives can be found in [28].

The simultaneous retrieval of the emissivity spectrum, skin temperature, and temperature,

water–vapor, and ozone atmospheric profiles is formulated within the context of optimal estimation [31]. The state vector, $\mathbf{v}$, is composed of an atmospheric component, $\mathbf{v}_1$, and an emissivity component, $\mathbf{v}_2$:

$$\mathbf{v} = (\mathbf{v}_1, \mathbf{v}_2)^t, \qquad (1)$$

where t means transpose. The size of the state vector will be denoted with N.

This state vector has to be derived from a set of independent observations of the spectral radiance, $R(\sigma)$. If the spectral radiance is observed at different wavenumbers σ_i, $i = 1, ..., M$, then the radiance vector, $\mathbf{R}$, is defined according to

$$\mathbf{R} = (R(\sigma_1), ..., R(\sigma_M))^t. \qquad (2)$$

Under the assumption of multivariate normality, our retrieval problem can be seen as one of optimal-estimation analysis in which a suitable estimation of the state vector is obtained by minimizing the cost function (e.g., [31–33])

$$\min_{\mathbf{v}} \left[\frac{1}{2} (\mathbf{R} - F(\mathbf{v}))^t \mathbf{S}_\varepsilon^{-1} (\mathbf{R} - F(\mathbf{v})) + \frac{1}{2} (\mathbf{v} - \mathbf{v}_a)^t \mathbf{S}_a^{-1} (\mathbf{v} - \mathbf{v}_a) \right]. \qquad (3)$$

In Eq. (3),

F: is the forward model function
$\mathbf{v}$: is the atmospheric state vector, of size N
$\mathbf{v}_a$: is the atmospheric background state vector, of size N
$\mathbf{S}_\varepsilon$: is the observational covariance matrix, of size $M \times M$
$\mathbf{S}_a$: is the background covariance matrix, of size $N \times N$

Note that our notation for background and observational vectors and covariances follows [31]. Furthermore, we use the symbol ϵ to index the observational covariance matrix, $\mathbf{S}_\epsilon$. This should not be confused with the symbol ε, which is used for emissivity.

For practical purposes, Eq. (3) has to be linearized in the forward model, so that its minimum can be sought through a Gauss–Newton iterative sequence. Linearization is obtained through Taylor-series expansion of $F(\mathbf{v})$ around a first-guess state vector $\mathbf{v}_0$:

$$\mathbf{R} = \mathbf{R}_0 + \left. \frac{\partial F(\mathbf{v})}{\partial \mathbf{v}} \right|_{\mathbf{v} = \mathbf{v}_0} (\mathbf{v} - \mathbf{v}_0) + \text{higher order terms}, \qquad (4)$$

where $\mathbf{R}_0 = F(\mathbf{v}_0)$. The introduction of the Jacobian,

$$\mathbf{K} = \left. \frac{\partial F(\mathbf{v})}{\partial \mathbf{v}} \right|_{\mathbf{v} = \mathbf{v}_0}, \qquad (5)$$

allows us to replace Eq. (3) with the quadratic form

$$\min_{x} \frac{1}{2} [(\mathbf{y} - \mathbf{Kx})^t] \mathbf{S}_\varepsilon^{-1} (\mathbf{y} - \mathbf{Kx}) + (\mathbf{x} - \mathbf{x}_a)^t \mathbf{S}_a^{-1} (\mathbf{x} - \mathbf{x}_a), \qquad (6)$$

where

$$\mathbf{y} = \mathbf{R} - \mathbf{R}_0,$$
$$\mathbf{x} = \mathbf{v} - \mathbf{v}_0,$$
$$\mathbf{x}_a = \mathbf{v}_a - \mathbf{v}_0. \qquad (7)$$

A. Forward Model

The forward model we use in this paper [34] solves the radiative transfer equation in the form

$$R(\sigma) = R_s(\sigma) + R_a(\sigma) + R_r(\sigma), \qquad (8)$$

where R is the upwelling radiance, decomposed in its surface term at the top of the atmosphere, R_s, atmospheric component, R_a, and surface reflected part, R_r, respectively. All quantities depend on the wavenumber σ, and the dependence over the directional angle is implicit.

In Eq. (8), the top-of-the-atmosphere surface term is

$$R_s(\sigma) = \varepsilon(\sigma) B(\sigma; T_s) \tau_0(\sigma) \qquad (9)$$

with

τ_0: the total transmittance of the atmosphere
ε: the emissivity spectrum
T_s: the skin temperature
B: the blackbody Planck function

The atmospheric component is dealt with in the usual way,

$$R_a(\sigma) = \int_0^{+\infty} B(\sigma, T) \frac{\partial \tau}{\partial h} \mathrm{d}h \qquad (10)$$

with h the vertical spatial coordinate and τ the transmittance from altitude h to $+\infty$. The term $R_r(\sigma)$ is appropriately dealt with according to the surface type. For sea surface, we use a specular model and [35]:

$$R_r(\sigma) = (1 - \varepsilon) \tau_0^2 \int_0^{+\infty} B(\sigma, T) \frac{1}{\tau^2} \frac{\partial \tau}{\partial h} \mathrm{d}h. \qquad (11)$$

For land, we use a Lambertian (diffuse) model and [35]:

$$R_r(\sigma) = \tau_0 (1 - \varepsilon) \int_{+\infty}^0 B(\sigma, T) \frac{\partial \tau_*^f}{\partial h} \mathrm{d}h \qquad (12)$$

with

$$\tau_*^f(h) = 2 \int_0^1 \tau_*(\mu, h)\mu \, d\mu, \tag{13}$$

where τ_* is the transmittance from altitude h to $h = 0$ along the slant path in the direction $\mu = \cos\theta$ (with θ the satellite zenith angle). The top-to-bottom transmittance τ_* should not be confused with the bottom-to-top transmittance τ.

According to [36], it is postulated that

$$\tau_*^f(\mu, h) = \tau_*(\bar{\mu}, h), \tag{14}$$

that is, the diffuse transmittance can be calculated as the transmittance function at a suitable cosine angle; the term $1/\bar{\mu}$ is referred to as the diffusivity factor. For practical calculations, the value $1/\bar{\mu} = 1.66$ (which corresponds to an effective zenith angle of 52.96 deg) yields accurate results. Actually, the accuracy depends on the optical depth. For optical depth below 1, exact and approximate [through Eq. (14)] calculations nearly coincide [37]. Using Eq. (14), for a Lambertian surface the reflected term, $R_r(\sigma)$, is computed according to

$$R_r(\sigma) = \tau_0(1 - \varepsilon) \int_{+\infty}^0 B(\sigma, T) \frac{\partial \tau_*(\bar{\mu}, h)}{\partial h} \, dh. \tag{15}$$

Our forward model, σ-IASI, computes $R(\sigma)$ at the monochromatic level. The monochromatic spectrum is convolved with the spectral response function of the given instrument (e.g., IASI) to obtain the appropriate spectral radiance.

In the present work, we assume that the reflected-sunlight term is negligible. This is generally a good approximation below 2230 cm^{-1}; however, under particular Sun–satellite geometry and with specular reflection, this term could yield an additional contribution to the brightness temperature spectrum of up to 0.4 K in the infrared atmospheric window [38]. Thus, on sea surface the use of observations at field-of-view angles close to the specular incidence of Sun angle should be avoided. For land, under the assumption of a Lambertian surface, the reflected sunlight term is also negligible within the infrared atmospheric window [38].

B. Including the Emissivity Spectrum within the State Vector

To retrieve the emissivity spectrum, we have to properly define and compute a linearized form of the forward model. We have

$$\mathbf{y} = \mathbf{Kx}, \tag{16}$$

where

$$\mathbf{K} = (\mathbf{K}_1, \mathbf{K}_2), \tag{17}$$

$$\mathbf{x} = \begin{pmatrix} \mathbf{x}_1 \\ \mathbf{x}_2 \end{pmatrix} = \begin{pmatrix} \mathbf{v}_1 - \mathbf{v}_{01} \\ \mathbf{v}_2 - \mathbf{v}_{02} \end{pmatrix}, \tag{18}$$

and subscripts 1 and 2 refer to the atmospheric and emissivity components, respectively. $\mathbf{K}_1$ is computed as usual by considering the derivative of the radiance, $R(\sigma)$, with respect to the atmospheric parameters.

In the same way, $\mathbf{K}_2$ is computed by differentiating $R(\sigma)$ with respect to emissivity. In doing so, we first transform emissivity using the logit function,

$$z(i) = \text{logit}(\varepsilon(i)) = \log\left(\frac{\varepsilon(i)}{1 - \varepsilon(i)}\right), \qquad i = 1, \dots, M, \tag{19}$$

which has inverse

$$\varepsilon(i) = \frac{\exp(z(i))}{1 + \exp(z(i))}, \qquad i = 1, \dots, M, \tag{20}$$

where, to simplify the notation, we have written $\varepsilon(i)$ instead of $\varepsilon(\sigma_i)$ and where, again, M is the number of radiance data points or channels. The logit transform allows us to work with a quantity, z, that is defined in the range $[-\infty, +\infty]$ and, hence, transform the emissivity, which is defined over the range $[0,1]$, to a new parameter for which the hypothesis of Gaussian shape is more realistic. Furthermore, the retrieval for the emissivity is forced to be in the interval $[0,1]$. Using the chain rule for the derivative of a composite function, we can write the Jacobian derivative with respect to z in terms of the Jacobian with respect to emissivity,

$$\frac{\partial R(i)}{\partial z(i)} = \frac{\partial R(i)}{\partial \varepsilon(i)} \left(\frac{\partial z(i)}{\partial \varepsilon(i)}\right)^{-1} = \frac{\partial R(i)}{\partial \varepsilon(i)} \varepsilon(i)(1 - \varepsilon(i)). \tag{21}$$

This allows us to easily linearize the forward model with respect to z,

$$\frac{\partial R(i)}{\partial z(i)}(z(i) - z_0(i)), \tag{22}$$

with z_0 a suitable first-guess point.

Second, we develop the z spectrum in a truncated Fourier cosine series, with truncation point $M_{\text{cut}} \le M$:

$$z(i) = \sum_{j=1}^{M_{\text{cut}}} w(j)c(j) \cos\frac{\pi(2i-1)(j-1)}{2M} \qquad i = 1, \dots, M, \tag{23}$$

with

$$w(j) = \begin{cases} \sqrt{1/M} & \text{for } j = 1 \\ \sqrt{2/M} & \text{for } j = 2, \dots, M_{\text{cut}} \end{cases} \tag{24}$$

where the coefficients $c(j)$ for any $j = 1, \dots, M$, can be computed according to

$$c(j) = w(j) \sum_{i=1}^{M} z(i) \cos \frac{\pi(2i-1)(j-1)}{2M}$$
$$i = 1, ..., M, \tag{25}$$

with

$$w(j) = \begin{cases} \sqrt{1/M} & \text{for } j = 1 \\ \sqrt{2/M} & \text{for } j = 2, ..., M \end{cases} \tag{26}$$

Third, inserting the truncated cosine transform within the linear term [Eq. (22)], we obtain

$$\frac{\partial R(i)}{\partial z(i)} \left(\sum_{j=1}^{M_{\text{cut}}} w(j)(c(j) - c_0(j)) \cos \frac{\pi(2i-1)(j-1)}{2M} \right), \tag{27}$$

which, defining

$$K_{2,ij} = \frac{\partial R(i)}{\partial z(i)} \left(w(j) \cos \frac{\pi(2i-1)(j-1)}{2M} \right), \tag{28}$$

can be put in the vector–matrix form

$$\mathbf{K}_2(\mathbf{c} - \mathbf{c}_0), \tag{29}$$

which shows that the *emissivity* state vector [indicated with $\mathbf{v}_2$ in Eq. (18)] is made up of the Fourier coefficients, $\mathbf{v}_2 \equiv \mathbf{c} = (c_1, ..., c_{M_{\text{cut}}})$.

Note that $\mathbf{K}_2$ is a matrix of size $M \times M_{\text{cut}}$ and $\mathbf{v}_2$ is a vector of size M_{cut}; therefore, if we use $M_{\text{cut}} \ll M$, we can achieve a large dimensionality reduction and represent the whole emissivity spectrum over, e.g., the IASI spectral coverage of 645–2760 cm^{-1} with a few Fourier coefficients.

It is important to stress that although the spectral decomposition of the emissivity is obtained over the whole IASI wavenumber range, we do not need to use all the IASI channels in a practical inversion of IASI radiances. We can consider a given set of channels, even not consecutive (although the penalty is a less accurate reconstruction of the emissivity spectrum). All we have to do is to select the same channels we use in the inversion process from the Jacobian, $\mathbf{K}_2$. That is, we have to use only the $\mathbf{K}_2$ rows that correspond to the channels selected for the retrieval. Nevertheless, the final estimate for the emissivity spectrum will be defined over the full 645–2760 cm^{-1} range. The data will contribute information at the channels we have used in the inversion; at other channels, this information will be that of the background vector (see next subsection), through interpolation by the Fourier cosine series.

It is also important to note that the appropriate M_{cut} depends on the kind of surface. As an example, for sea surface we expect a smooth behavior along the IASI spectral coverage, which is well represented, e.g., by the model of [39]. Figure 1 shows the

representation of the sea-surface Masuda model for emissivity with $M_{\text{cut}} = 20$, 40, and 60. It can be seen that with $M_{\text{cut}} \geq 40$ we can represent all the important features of the sea emissivity spectrum. Conversely, in case we want to represent the features exhibited by a quartz-rich sand (see Fig. 2), we need 400 Fourier coefficients in order to fully recover the 8–10 μm (1000–1250 cm^{-1}) reststrahlen doublet of quartz.

The examples provided in Figs. 1 and 2 show how we can improve the spectral resolution of the Fourier expansion by just increasing the number of harmonics in the series. In this respect, one could consider that the emissivity spectrum is a *spectrum* for which we can use the mathematical machinery of Fourier spectroscopy [40], which, in turn, allows us to *spectrally* define emissivity. In fact, the Fourier
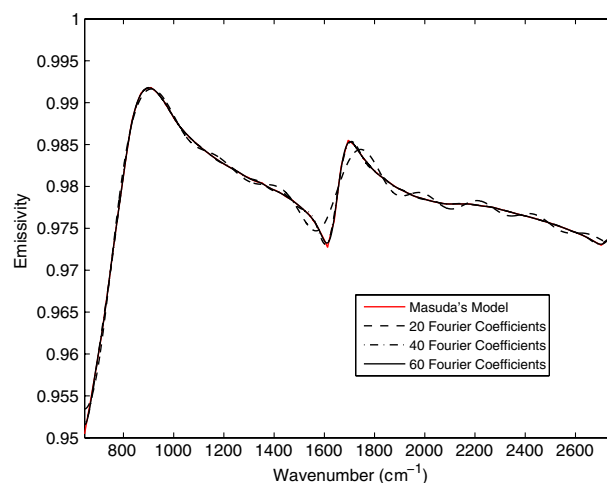
Fig. 1. Masuda model for the sea emissivity spectrum and its representation with 20, 40, and 60 Fourier coefficients.
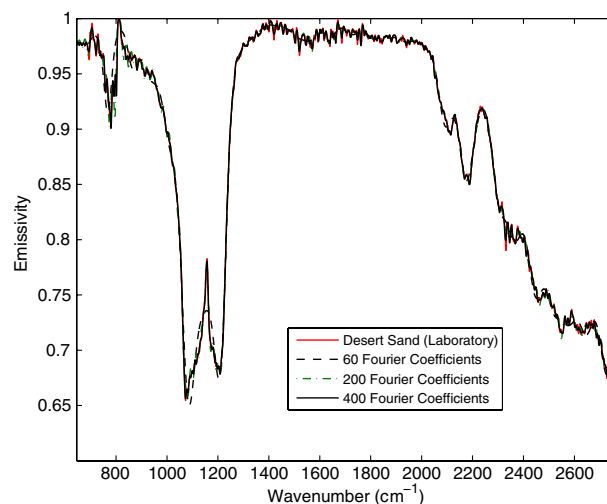
Fig. 2. Desert-sand emissivity spectrum (laboratory measurement from MODIS group of Institute for Computational Earth System Science, UCSB, http://www.icess.ucsb.edu/modis/EMIS/html/em.html) and its representation with 60, 200, and 400 Fourier coefficients.

coefficients of the expansion can be interpreted the same way as we do with a genuine light spectrum, that is, they are interferogram samples. If we retain M_{cut} values only of the expansion, the spectral resolution of emissivity spectrum, rendered through the truncated expansion, will be simply scaled by the factor M/M_{cut}. In other words, let us assume that the spectral resolution of the emissivity spectrum represented with all the M harmonics is $\delta\sigma_\varepsilon$; the spectral resolution corresponding to M_{cut} is

$$\frac{M}{M_{cut}}\delta\sigma_\varepsilon. \tag{30}$$

To be more precise, in this case it would be more appropriate to speak of spectral sampling rather than spectral resolution; however, this does not change the basic formula shown above.

Based on Eq. (30), we can now understand that in Fig. 1, $M_{cut} = 60$ corresponds to the relatively low spectral sampling of ≈ 35 cm^{-1}. This sampling should be enough to represent smooth structure expected for sea-surface emissivity. In contrast, for desert sand we need to improve the sampling, because we have to resolve structures such as the peak at 1160 cm^{-1} of the reststrahlen doublet of quartz. In fact, we use $M_{cut} = 400$, which corresponds to a sampling of about 5 cm^{-1}.

It is also important to stress that our way to represent the emissivity spectrum is consistent with the Shannon–Whittaker sampling theorem [41]; therefore, under the assumption that the emissivity spectrum $\varepsilon(\sigma)$ is bandlimited and sampled at a high enough rate, $\delta\sigma_\varepsilon$, our Fourier-transform formalism provides an interpolation formula, which is guaranteed to reconstruct it exactly. This property

is not guaranteed in case one uses, e.g., principal-component analysis, or other *ad hoc*, subjective, ways to sample the emissivity spectrum. It is important to stress that by the "IASI spectrum," we mean the measurement is band limited and, *a fortiori*, the emissivity spectrum, which we retrieve from the IASI spectrum.

C. Constraining the Inverse Solution

In the same way we do with atmospheric parameters, the emissivity spectrum is constrained with a suitable background built upon a suitable ensemble of emissivity spectra. These can be derived from laboratory measurements [1] and, eventually, in a case of composite scenes, synthesized together with an appropriate bidirectional reflectance distribution function model [42]. For our analysis, appropriate emissivity ensembles are obtained by the ASTER (Advanced Spaceborne Thermal Emission Reflection Radiometer) Spectral Library, version 2.0 [43], and the MODIS (Moderate Resolution Imaging Spectrometer) UCSB (University of California, Santa Barbara) Emissivity Library (http://www.icess.ucsb.edu/modis/EMIS/html/em.html).

Depending on the scene, the appropriate ensemble is then used to obtain the background, $\mathbf{v}_a^{(2)}$, and its covariance matrix, $\mathbf{S}_a^{(2)}$. We assume that the covariance matrix is diagonal, and therefore we compute the sample variance of the emissivity spectrum at each wavenumber. The background $\mathbf{v}_a^{(2)}$ is the vector of the Fourier coefficients, whereas $\mathbf{S}_a^{(2)}$ is the variance of the Fourier coefficients.

The background vector $\mathbf{v}_a^{(2)}$ and its sample standard deviation is exemplified in Fig. 3 for three cases: sea surface, desert sands, and savanna. In this figure we show the Fourier coefficients corresponding to the
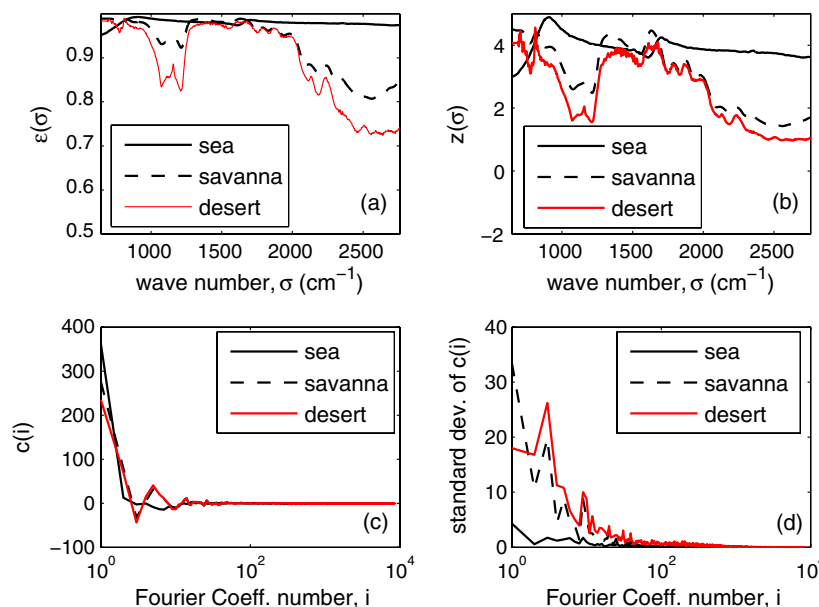

Fig. 3. Background emissivity for three surface types: sea, savanna, and desert. (a) Emissivity spectrum. (b) Logit transform of emissivity. (c) Fourier coefficients of the discrete cosine transform of $z(\sigma)$. (d) Standard deviation of the Fourier coefficients.

full IASI spectral coverage 645–2760 cm^{-1} for a total of $M = 8461$ coefficients. In practice, when we consider the retrieval problem we truncate the expansion at a given M_{cut}. For the cases shown in this paper, sea surface and desert sand, we have 60 for sea emissivity and 400 for the case of desert land. The background vector and covariance shown in Fig. 3 were obtained from 38 desert laboratory samples in the case of desert sand. For sea surface, we have eight seawater laboratory samples together with eight more samples from Masuda's model [39] with wind speed in the range 2.5–20 m/s (steps of 2.5 m/s). These eight samples are further expanded by considering related computations as a function of the 15 IASI fields of view. For desert and sea surface, we have not used or applied any kind of scene synthesis, since we assume that we are dealing with homogeneous scenes. For the savanna, we consider a scene synthesis through the method developed in [42], in which we consider three basic components: desert sand, grass, and trees/brushes. Sand and grass are combined through a volumetric model to have the basic ground, which is further combined in a geometric model with tree-foliage emissivity to obtain the final composite emissivity. We have eight components for desert sand, two for grass (dry and green), and one for leaf (this is just an average of the leaf emissivity in our database). However, the synthesis has been done by changing abundance of the three components and model parameters, in such a way as to have 100 emissivity samples that are used to yield the background shown in Fig. 3. It is possible that the background shown in Fig. 3 is not optimal for the given surface. They are here mostly intended to exemplify our methodology. Different strategies could be considered for building the background, which may depend on the user. In this respect, the software we have developed accepts any user-defined background.

The background covariance matrix for the atmospheric parameters will be denoted by $\mathbf{S}_a^{(1)}$. We do not consider correlation between atmospheric parameters and emissivity spectrum; therefore, the whole covariance matrix is obtained as

$$\mathbf{S}_a = \begin{pmatrix} \gamma_1^{-1}\mathbf{S}_a^{(1)} & \mathbf{0} \\ \mathbf{0} & \gamma_2^{-1}\mathbf{S}_a^{(2)} \end{pmatrix}. \tag{31}$$

Because of the block-diagonal form, we have

$$\mathbf{S}_a^{-1} = \begin{pmatrix} \gamma_1(\mathbf{S}_a^{(1)})^{-1} & \mathbf{0} \\ \mathbf{0} & \gamma_2(\mathbf{S}_a^{(2)})^{-1} \end{pmatrix}. \tag{32}$$

The parameters γ_1 and γ_2 are two extra regularization parameters, which can be suitably tuned to balance the constraints. This balancing is particularly appropriate for the emissivity spectrum, since $\mathbf{S}_a^{(2)}$ could be noncommittal for the given data, reflecting the poor *a priori* information we have for land surface. The use of two parameters allows us to

introduce an extra smoothing for the emissivity spectrum, which is independent of the atmospheric parameters and vice versa.

Another useful form of Eq. (32) makes use of the diagonal matrix $\mathbf{\Gamma}$, whose diagonal elements are equal to γ_1 for the rows corresponding to the atmospheric parameters and γ_2 for the rows corresponding to the emissivity spectrum. If we define

$$\tilde{\mathbf{S}}_a^{-1} = \begin{pmatrix} (\mathbf{S}_a^{(1)})^{-1} & \mathbf{0} \\ \mathbf{0} & (\mathbf{S}_a^{(2)})^{-1} \end{pmatrix}, \tag{33}$$

then

$$\mathbf{S}_a^{-1} = \mathbf{\Gamma}\tilde{\mathbf{S}}_a^{-1}, \tag{34}$$

The two parameters can be fixed in many ways. We could just use $\gamma_1 = 1$ if we knew that $\mathbf{S}_a^{-1}$ is a good constraint, and try to optimize γ_2. In case we have good *a priori* information for the emissivity spectrum (e.g., for sea surface we know that Masuda's model is a very good *a priori*), we could set γ_2 equal to a very large values and try to optimize with respect to γ_1. In any case, the introduction of two parameters in the scheme gains us flexibility and allows us to deal with the two characteristics of the retrieval problem, atmosphere and surface, separately.

The two parameters, γ_1 and γ_2, can be also determined through objective procedures such as the L-curve method [30]. The calculations provided in Appendix A show how to implement an analytical 2D L-curve criterion for the objective computation of γ_1 and γ_2.

D. The *a posteriori* Covariance Matrix

Because we have two regularization parameters, the *a posteriori* covariance matrix, $\hat{S}_c$ of the estimated state vector is not that normally derived within the optimal-estimation methodology [31]. The appropriate expression of the *a posteriori* covariance matrix can be obtained by generalizing the one-dimensional L-curve case shown in [44]. The result for our 2D case reads

$$\hat{\mathbf{S}}_c = \mathbf{S}_\nu^{-1}(\mathbf{\Gamma}^2\tilde{\mathbf{S}}_a^{-1} + \mathbf{K}^t\mathbf{S}_\epsilon^{-1}\mathbf{K})\mathbf{S}_\nu^{-1} \tag{35}$$

with

$$\mathbf{S}_\nu = (\mathbf{\Gamma}\tilde{\mathbf{S}}_a^{-1} + \mathbf{K}^t\mathbf{S}_\epsilon^{-1}\mathbf{K}), \tag{36}$$

which for $\mathbf{\Gamma} = \mathbf{I}$ reduces to the usual form of the *a posteriori* matrix for Rodgers's regularization [31],

$$\hat{\mathbf{S}}_c = (\mathbf{S}_a^{-1} + \mathbf{K}^t\mathbf{S}_\epsilon^{-1}\mathbf{K})^{-1}, \tag{37}$$

The *a posteriori* covariance matrix $\hat{S}_c$ applies to the atmospheric parameters and the Fourier coefficients of the logit-transformed emissivity spectrum. To have the covariance in the physical emissivity space, the above covariance matrix has to be properly transformed. The transformation can be obtained in

two steps. First, consider that the cosine transform of Eq. ([23](#)) can be written in a vector–matrix formalism as

$$\mathbf{z} = \mathbf{A}_F \mathbf{c}, \tag{38}$$

where the Fourier-coefficients vector $\mathbf{c}$ has size M_{cut}, $\mathbf{z}$ has size M, and the Fourier kernel $\mathbf{A}_F$ has size $M \times M_{cut}$ and has elements defined by

$$\mathbf{A}_{F;ij} = w(j) \cos \frac{\pi(2i-1)(j-1)}{2M},$$
$$i = 1, ..., M; j = 1, ..., M_{cut}, \tag{39}$$

Thus, the transform from the whole state vector (atmopshere + emissivity) with c-elements to that with z-elements reads

$$\begin{pmatrix} \mathbf{v}_1 \\ \mathbf{z} \end{pmatrix} = \begin{pmatrix} \mathbf{I}_1 & \mathbf{0} \\ \mathbf{0} & \mathbf{A}_F \end{pmatrix} \begin{pmatrix} \mathbf{v}_1 \\ \mathbf{c} \end{pmatrix}, \tag{40}$$

where $\mathbf{I}_1$ is the identity matrix.

If we define

$$\mathbf{A}_T = \begin{pmatrix} \mathbf{I}_1 & \mathbf{0} \\ \mathbf{0} & \mathbf{A}_F \end{pmatrix}, \tag{41}$$

then the covariance matrix corresponding to the z-elements is given by

$$\hat{\mathbf{S}}_z = \mathbf{A}_T \hat{\mathbf{S}}_c \mathbf{A}_T^t \tag{42}$$

It should be noted that this matrix has size $(M + N_1) \times (M + N_1)$.

Second, from the logit transform we learn that a variation in the emissivity at channel i, that is, $\Delta\varepsilon(i)$, corresponds to a variation $\Delta z(i)$ according to

$$\Delta\varepsilon(i) = (1 - \varepsilon(i))\varepsilon(i)\Delta z(i). \tag{43}$$

Let us define the diagonal matrix, Δ according to

$$\Delta_{ii} = \begin{cases} 1, & i = 1, ..., N_1, \\ (1 - \varepsilon(i - N_1))\varepsilon(i - N_1), & i = N_1 + 1, ..., M + N_1, \end{cases} \tag{44}$$

then the final *a posteriori* covariance matrix, $\hat{\mathbf{S}}$, for the atmospheric and emissivity elements is given by

$$\hat{\mathbf{S}} = \Delta \hat{\mathbf{S}}_z \Delta^t. \tag{45}$$

3. Results

We first briefly summarize the other ingredients of the inverse scheme, which apply to the atmospheric parameters. For these parameters, including skin temperature, a first guess to initialize the retrieval scheme is obtained with an empirical orthogonal functions (EOF) regression. We note that the EOF regression is not used for emissivity. In this case, the emissivity first guess is shown in Fig. [3](#) for the two surface coverages analyzed in this paper, namely, sea and desert sand.

Methodology and validation of the scheme for the atmospheric parameters have been described in many papers [[44–51]](#), to which the reader is referred for further details. For brevity, we limit ourselves to the performance of the scheme. For sea surface, the temperature retrieval is accurate within ± 1 K in the troposphere. An accuracy of 10%–15% for humidity is observed in the middle-to-lower troposphere. For land surface, recent results from the COPS (Convective and Orographically induced Precipitation Study) campaign in Germany [[52,53]](#) show that our retrieval for temperature compares within 1–2 K with radiosonde and lidar observations, whereas the agreement for humidity is within 10%–20% in the lower troposphere.

The present approach, including emissivity retrieval, can be applied to clear and cloud-cleared radiances for both daytime and nighttime. Because solar radiation can contribute to the observed infrared radiance in the shortwave spectral region, only channels below 2230 cm^{-1} are used for daytime processing. However, for nighttime the complete IASI coverage can be used. For the present analysis, daytime IASI spectra have been considered, and the spectral interval used for retrieval covers the two ranges 645–1250 and 1450–2230 cm^{-1}.

A. Application to IASI Soundings over Sea Surface

Sea surface is a good benchmark to check the performance of the retrieval of the emissivity spectrum, because it provides a homogeneous scene for which, as already stated, Masuda's model [[39]](#), parameterized for viewing angle and surface roughness, has been used successfully and extensively in satellite retrieval algorithms.

IASI spectra for sea surface have been derived from the Joint Airborne IASI Validation Experiment (JAIVEx) [[54]](#), which was carried over the Gulf of Mexico during April and May 2007. We have a series of six spectra for the day 29 April 2007, which were recorded at nadir, and 19 spectra for 30 April 2007 and 4 May 2007, which were recorded with a field-of-view angle of 22.5 deg. The IASI spectra are clear-sky sea-surface measurements, and they are complemented with dropsonde observations for temperature, water vapor, and ozone and forecasts from the European Centre for Medium-Range Weather Forecasts (ECMWF). Sea-surface skin temperature was also derived from ARIES (Airborne Research Interferometer Evaluation System; see, e.g., [[12]](#)) radiances. During the JAIVEx experiment, AIRES was flown on board the United Kingdom Meteorological Office FAAM (Facility for Airborne Atmospheric Measurements) BAe (British Aerospace) 146 research aircraft.

Figure [4](#) summarizes the results for the retrieval of skin temperature. The scatterplot in Fig. [4(a)](#) shows that the retrieval for skin temperature, T_s, does not change in case we impose Masuda's model (for a wind
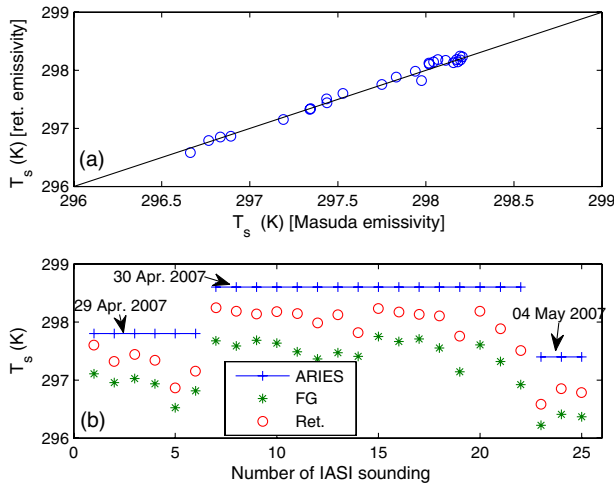
Fig. 4. Retrieved skin temperature for sea surface. (a) Scatterplot between T_s obtained by imposing Masuda's model over the retrieval and that obtained by simultaneously retrieving emissivity and T_s. (b) Comparison with the ARIES retrieval for the 3 days considered in the exercise. In the key, "FG" stands for first guess and "Ret." for retrieval.

speed of 5 m/s) and retrieve only T_s or we simultaneously retrieve emissivity and T_s. The standard deviation and bias of the difference between the two retrievals shown in Fig. 4(a) is of the order of 0.01 K. A comparison of the retrieved skin temperature derived from ARIES (the Airborne Research Interferometer Evaluation System; see, e.g., [12]) retrievals, averaged over the intensive-measurement JAIVEx target area, is shown in Fig. 4(b) for the 3 days for which we have the IASI soundings. The mean difference between IASI and ARIES retrievals is −0.51 K for 29 April 2007, −0.58 K for 30 April 2007 and −0.64 K for 4 May 2007. The imperfect overlap between ARIES and IASI spatial patterns has to be kept in mind when considering these differences.

Figure 5 provides a comparison of the retrieved emissivity spectrum (nadir observations) with the corresponding Masuda model for a wind speed of 5 m/s. The retrieval has been averaged over the six nadir IASI soundings, and the error bars shown in this figure were computed according to the square root of the diagonal of Eq. (45). In addition, they were properly scaled to take into account the average operation (division by the square root of the number of samples). The figure also shows the IASI spectral ranges, which were not used in the inversion.

Of course, differences between model and retrieval are most significant in those spectral ranges, which were used for the retrieval, because in the other ranges the retrieval is an extrapolation obtained with a truncated cosine series (see, e.g., Subsection 2.B).

A slight discrepancy exists in the 1000–1200 cm^{-1} window region. This is confirmed by analyzing the IASI observations at 22.5 deg (Fig. 6), although as shown in Fig. 4, the magnitude of the discrepancy is too small to be of relevance for the retrieval for the skin temperature.
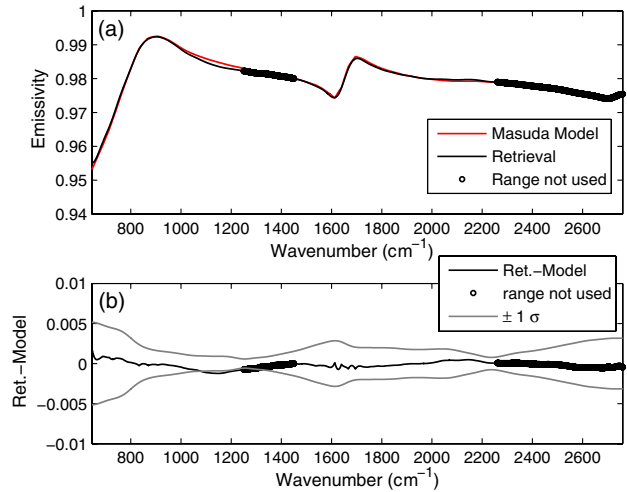

Fig. 5. Comparison of the retrieved emissivity spectrum and Masuda's model for a series of six IASI soundings at nadir. The retrieval has been averaged over the six soundings. The circles individuate the spectral ranges, which were not used in the retrieval analysis. (a) Comparison between the retrieved and modeled emissivity spectra. (b) Retrieval-minus-model difference and the corresponding error bars.

The IASI soundings at 22.5 deg show a slight but systematic discrepancy in the CO_2 band at 14 μm, where the model indicates a slightly lower emissivity than the retrieval. This behavior is reflected in the retrieval for temperature, which seems to improve when we simultaneously retrieve it with the emissivity spectrum. The effect is much more evident for the retrievals corresponding to the three IASI soundings on 4 May 2007. These are shown in Fig. 7 for the case in which we retrieve temperature with the Masuda model and the case for which both are retrieved simultaneously. However, the statistics are too poor to derive firm conclusions, and the example is here shown just to illustrate potential retrieval improvements with the present methodology in which the emissivity spectrum is simultaneously retrieved with the atmospheric parameters.
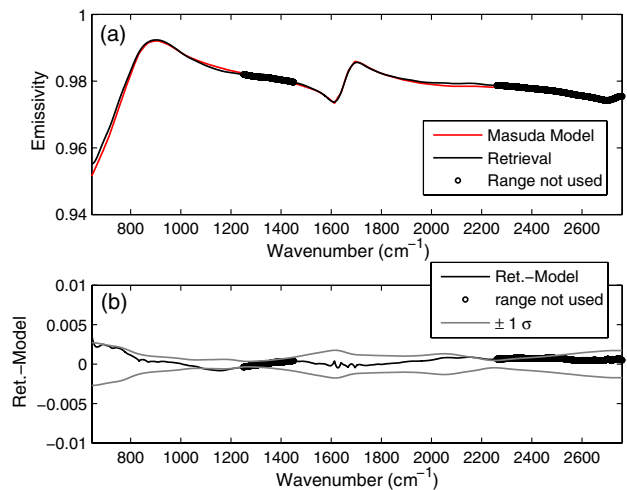

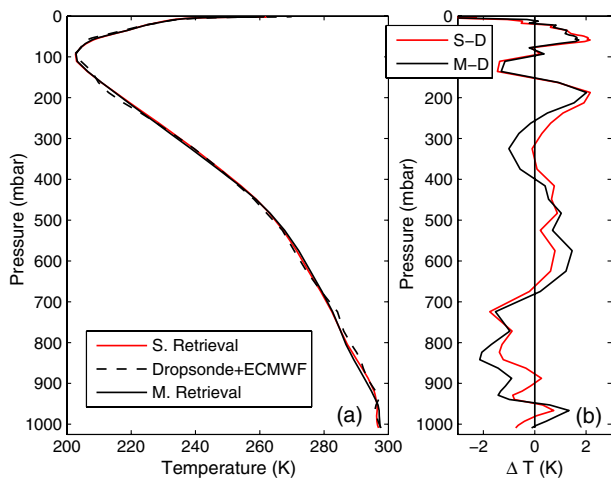Fig. 6. Same as Fig. 5, but for the series of 19 IASI soundings at a viewing angle of 22.5 deg.

Fig. 7. Mean-temperature retrieval over the three IASI soundings at viewing angle of 22.5 deg on 4 May 2007. (a) Comparison of the dropsonde (extended with ECMWF forecast above 400 hPa) profile with that simultaneously retrieved with the emissivity spectrum ("S. Retrieval") and that assuming the Masuda model for emissivity ("M. Retrieval"). (b) Illustration of the bias, where "S-D" refers to S. Retrieval—(dropsonde + ECMWF) and "M-D" to M. Retrieval—(dropsonde + ECMWF).

B. Application to IASI Soundings over Desert Sand

In this section, the methodology will be exemplified with IASI soundings over desert regions. We have considered IASI overpasses over the Namib and the Sahara Deserts.

For the Namib Desert we have a series of eight IASI spectra recorded at viewing angles between 41 and 46 deg [Fig. 8(b)]. The sands and dune fields of the Namib Desert have little vegetative cover, so their main spectral features are due to the rich content of quartz. The grain size of quartz is, for almost 70%, in the range below 250 μm [21,55,56]. This abundance of fine-grain-size particles yields an emissivity spectrum with a characteristic fingerprint within the reststrahlen band at 8.6 μm (1162.8 cm^{-1}). Thus, the Namib Desert overpasses can be used as a benchmark to check the retrieval quality of the emissivity spectrum, in the sense that the emissivity-spectrum retrieval must show this characteristic fingerprint.

A typical emissivity spectrum of fine-grained quartz sand is shown in Fig. 2. Within the reststrahlen band at 8.6 μm (1162.8 cm^{-1}), the emissivity is characterized by two local minima (at 8.27 μm, 1209.2 cm^{-1}, and 9.32 μm, 1073 cm^{-1}) of which the deepest occurs at 9.32 μm (1073 cm^{-1}. This structure tends to reverse with coarse-grained particulate (range of grain size 250–1500 μm), where the deepest minimum occurs at 8.27 μm (1209.2 cm^{-1}) [1]. Thus, by looking at the slope of these two minima we can get insight into the grain size of the quartz sand.

For the Sahara Desert, we analyze a full IASI scan line consisting of 120 spectra [Fig. 8(a)]. The spectra were recorded on 22 July 2007, during a morning orbit at 08:25 UTC. The scene variability for the Sahara Desert is much more pronounced than that for the Namib Desert. The IASI overpass covers sand seas and regions with a large variety of bulk mineralogy. However, the most abundant mineral is quartz, which means that the emissivity retrieval has to show the characteristic fingerprint of the reststrahlen band at 8.6 μm (1162.8 cm^{-1}).

The analysis for the Sahara Desert is intended to show the capability of our methodology to derive atmospheric parameters (temperature, water–vapor,

Fig. 8. (a) Sahara target area showing the IASI footprints (circles). (b) Namib target area showing the IASI footprints (circles). (c) Sahara target area (Ouargla Province, Algeria) showing the SEVIRI pixels (square boxes) and the colocated IASI footprints.

and ozone profiles), in addition to the emissivity spectrum. This is particularly interesting for a desert site for which we know that Numerical Weather Prediction models fail to be accurate in the lower troposphere and tend to largely underestimate the skin temperature, because of poor emissivity parameterizations. The retrieval will be compared with time–space colocated profiles from the ECMWF (analysis) model.

For the case of the Sahara Desert, further IASI observations, colocated with *Meteosat* Second Generation SEVIRI (Spinning Enhanced Visible and Infrared Imager) instrument, will be analyzed to specifically compare emissivity and skin-temperature products. The target area for this intercomparison exercise is shown in Fig. 8(c). The target area is geographically located in Ouargla Province, Algeria. We have 14,266 SEVIRI pixels covering the target area (the SEVIRI pixel is a box of 3 km × 3 km). A number of 123 IASI soundings have been time- and space-colocated with the SEVIRI pixels, as shown in Fig. 8(c). SEVIRI observations (*Meteosat-9* high-rate SEVIRI level 1.5 image data) have been acquired on 4 July 2010, 10:07:00 UTC, whereas the IASI observations refer to the same day, 10:00:21 UTC.

1. Namib Desert

The results for the emissivity spectrum are shown in Fig. 9. It can be seen that we retrieve the expected reststrahlen-band positive slope, which characterizes quartz-rich sand with fine-grained particles. Similar results have been previously reported in [21]. We stress here that the background emissivity we have used for the present exercise is that shown in Fig. 3, which has just the opposite (negative) slope in comparison with the retrieval shown in Fig. 9. The result exemplifies that our methodology is capable of retrieving genuine features in the data and not in the background.
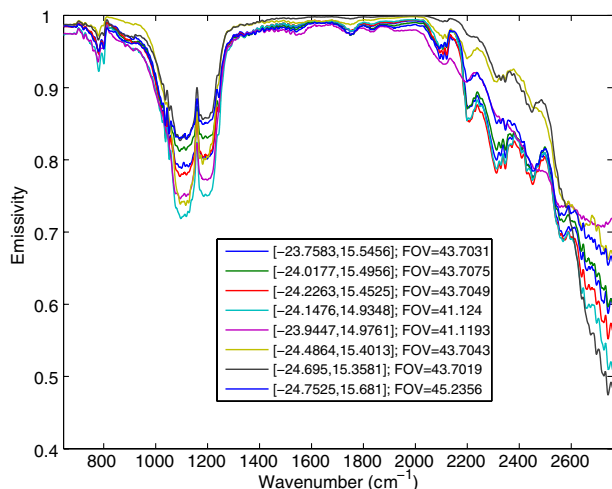

Fig. 9. Emissivity retrieval for the Namib Desert case study. The position (latitude, longitude in degrees) and the field of view (FOV, in degrees) of each sounding are shown in the key.
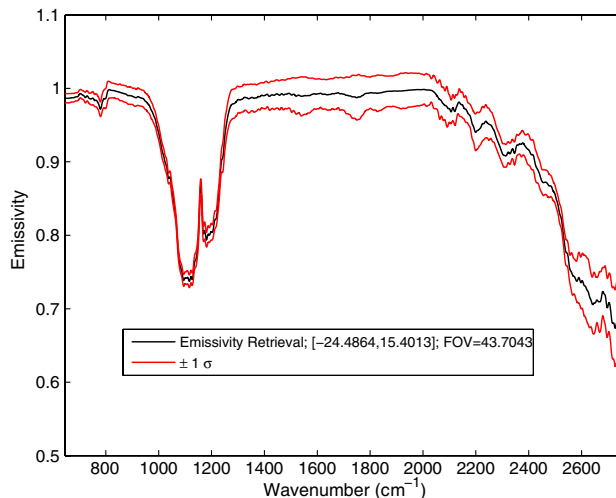

Fig. 10. Exemplification of the retrieval precision for the emissivity spectrum over desert soil. For one of the spectra shown in Fig. 8 the figure shows the $\pm 1\,\sigma$ tolerance interval, computed according to Eq. (45). The key gives the position (latitude, longitude in degrees) and the field of view (FOV, in degrees) of the sounding.

This is the main result we wanted to achieve in the case of the Namib Desert. It should be noted that the large variability of the emissivity spectra shown in Fig. 9 is a consequence of the scene variability in the IASI footprints (Fig. 8). In addition, Fig. 10 exemplifies the retrieval precision for the whole emissivity spectrum. The precision is computed as the square root of the diagonal elements of the covariance matrix provided by Eq. (45).

2. Sahara Desert

The IASI spectra analyzed for the Sahara Desert belong to a full scan line (120 soundings) for an east-to-west swath length of ≈ 2400 km [Fig. 8(a)]. The emissivity retrieval shows a larger variability than the case corresponding to the Namib Desert, although the signature of the reststrahlen band is quite visible in each single retrieval.

This is exemplified in Fig. 11 for three different IASI soundings. The sounding (latitude 28.27 deg, longitude 23.86 deg), which shows the typical fingerprint of the fine grain size of quartz sand is located in the so-called great sea of sand. According to [57], this region is characterized by sand dunes with fine-grained particles.

As for the retrieval over sea surface, we can obtain a representation of the retrieved emissivity spectrum over the full IASI range, 645–2760 cm^{-1}, although the IASI spectral ranges used for the inversion covers the wavenumbers 645–1250 and 1450–2230 cm^{-1}. As stated in Section 3, the IASI segment 2230–2760 cm^{-1} is not used; hence, the emissivity in this range has no information from the data points. Furthermore, there are spectral ranges in the IASI spectra that are completely blind to the surface. This is the case, e.g., for the spectral range 1450–1900 cm^{-1}. It is important to stress that for ranges
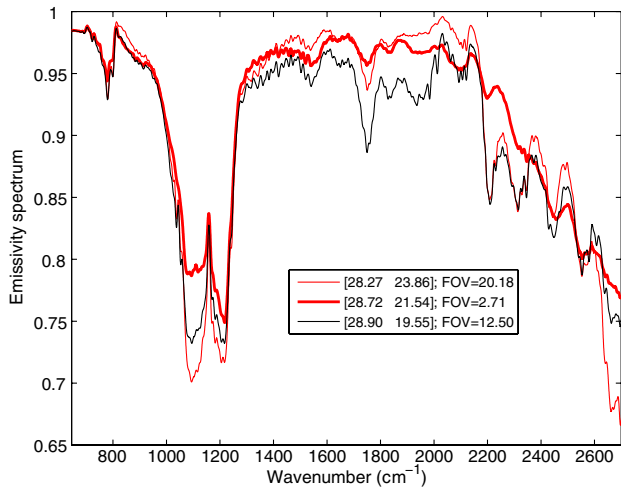
Fig. 11. Sahara Desert case study: emissivity-spectrum retrieval for three different soundings, exemplifying the presence of fine- and coarse-grained quartz particles. The position (latitude, longitude in degrees) and the field of view (FOV, in degrees) of each sounding are shown in the key.

either not used or blind to the surface, emissivity information comes form the background vector (that is, the set of laboratory measurements). Therefore, the pronounced dip at 1753 cm^{-1} of one of the emissivity spectra shown in Fig. 11 is a result of the variability of the background vector. In sum, for spectral ranges for which we do not have information from IASI we fill with the background-emissivity vector.

Figure 12 shows a map of the ECMWF and retrieved skin temperature. It can be seen that the two maps follow the same east-to-west decreasing pattern, which is, of course, in agreement with the east-to-west apparent Sun motion. However, it is clear that the ECMWF analysis is biased downward with respect to the retrieval. This bias is not an artifact of the retrieval, as can be seen from Fig. 13, which compares one individual IASI spectrum to that calculated with the ECMWF analysis profile.
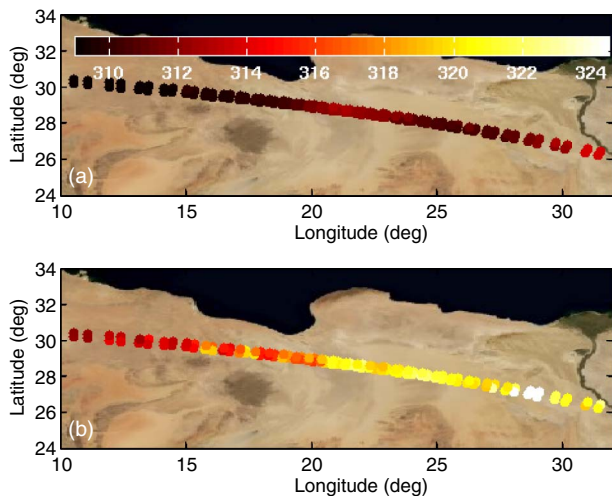

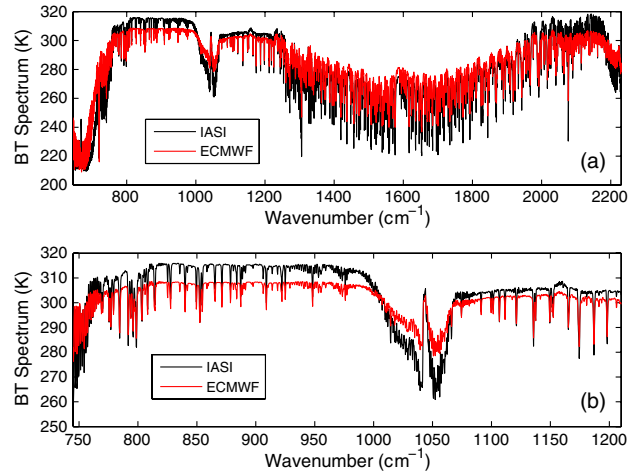Fig. 12. Sahara Desert case study: map of skin temperature. (a) ECMWF. (b) IASI retrieval.

Fig. 13. Sahara Desert case study: comparison for a single IASI footprint of the observed spectrum with the calculation performed with the skin temperature, temperature profile, water–vapor profile, and ozone profile derived from the ECMWF analysis. (a) 645–2230 cm^{-1}. (b) Atmospheric window. The field-of-view angle is 1.43 deg.

For the calculation we used the desert emissivity shown in Fig. 3(a). This emissivity could not be properly adequate; however, it should be stressed that at 833 cm^{-1} the emissivity is almost equal to unity even for desert sand. Nevertheless, at 833 cm^{-1} the difference in brightness temperature between IASI and ECMWF-based calculation is larger than 7 K.

Figures 14–16 compare the retrieval with the ECMWF analysis for temperature, water vapor, and ozone, respectively. For temperature, a large discrepancy is seen near the surface. This discrepancy tends to be confined within $\pm(1-2)$ K in the troposphere. However, a relatively high discrepancy is also seen at the tropopause level. Retrieval and ECMWF agree with each other as far the tropopause height is
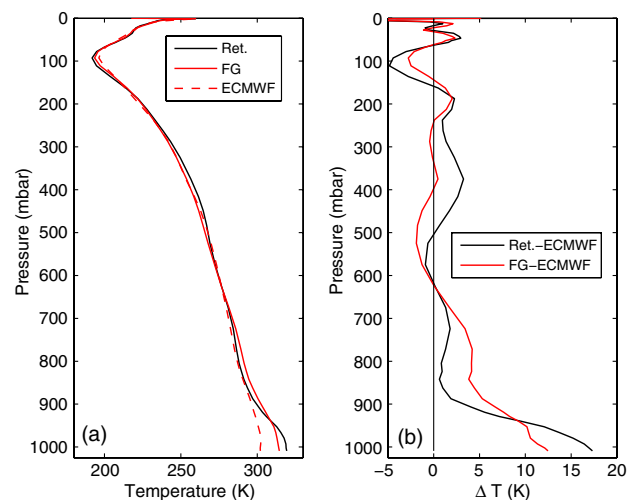

Fig. 14. Sahara Desert case study: temperature retrieval and comparison with the ECMWF analysis and the first guess. (a) Profiles. (b) Differences retrieval–ECMWF and (first guess)–ECMWF. The results have been averaged over the 120 corresponding profiles.
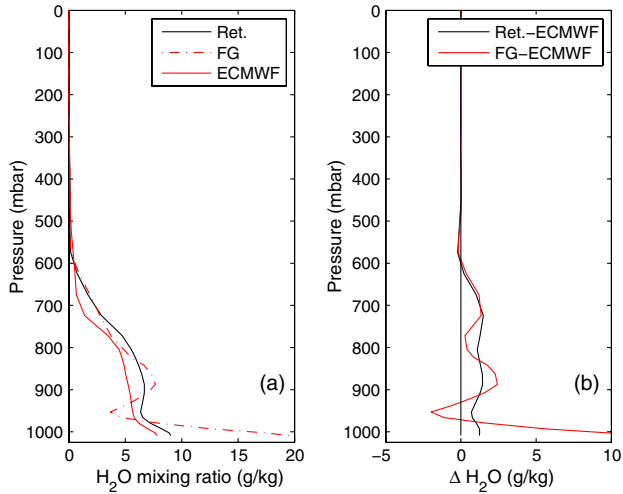
Fig. 15. Same as Fig. 14, but for water vapor.

Fig. 17. Sahara Desert case study. (a) Observed and retrieved spectrum in the range 645–1250 cm^{-1}. (b) Spectral residual: observed minus retrieved and observed minus first guess. The results have been averaged over the 120 IASI soundings.

concerned. However, the retrieval shows a tropopause that is colder by about 5 K than the ECMWF analysis. Keeping in mind the comparison shown in Fig. 13, from which we see that ECMWF shows a systematically warmer CO_2 band in the 700–780 cm^{-1} range, we think that this is not an artifact of the retrieval. For water vapor, we see a systematic discrepancy in the lower part of the troposphere, although differences are confined to within 1 g/kg. A discrepancy of ±1 ppmv (parts per million by volume) is also seen for ozone.

As a final check of the quality of our retrieval, Fig. 17 shows the behavior of the spectral residual over the range 650–1250 cm^{-1} we have used for the inversion. The range 1450–2230 cm^{-1} is shown in Fig. 18. It can be seen that the spectral residual is greatly reduced in comparison with the first guess. Figure 17 allows one to appreciate the goodness of the fit achieved in the atmospheric window region, notably in the spectral range from 1100 to 1200 cm^{-1}, which is the core of the reststrrahlen band of quartz. The quality of the fit at the emission peak of this band, that is, at ≈1160 cm^{-1}, is impressive.
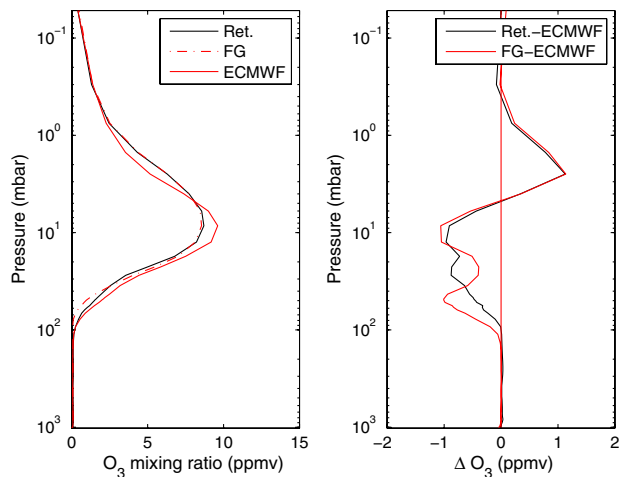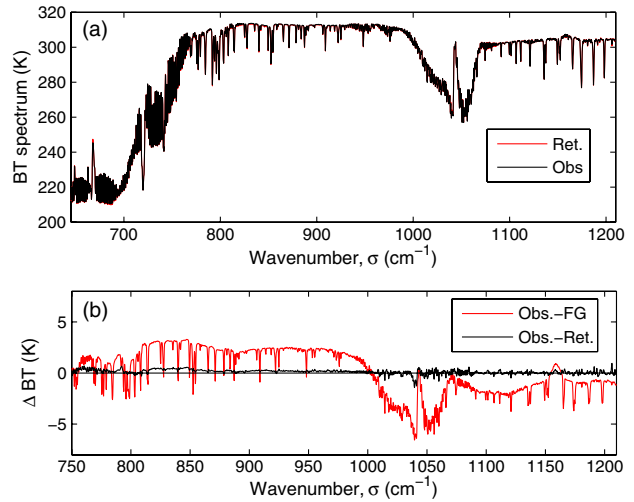
The goodness of the fit in the ozone band at 1045 cm^{-1} (9.6 µm) is also noteworthy. This good fit has been recently confirmed with ground-based Fourier transform spectrometer observations [58] and gives increased credit to the large improvement achieved by state-of-art O_3 spectroscopy in fitting the ozone absorption band at 9.6 µm [59].

3. SEVIRI versus IASI T_s − ε retrieval

In this subsection, we present and describe a SEVIRI-to-IASI comparison of emissivity and skin-temperature products. SEVIRI channel emissivity was retrieved at the three SEVIRI atmospheric window channels, 12, 10.8, and 8.7 µm (833.33, 925.92, and 1114.94 cm^{-1}, respectively) simultaneously with T_s, using a Kalman-filter approach [60]. To have a proper comparison with IASI emissivity retrieval, this has been transformed to SEVIRI-like channel
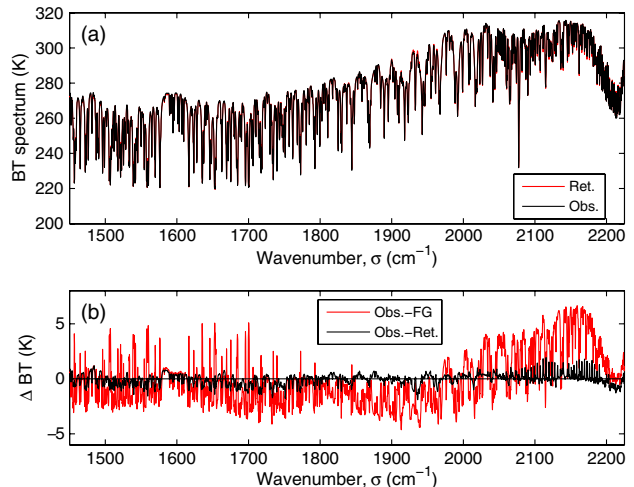

Fig. 16. Same as Fig. 14, but for ozone.
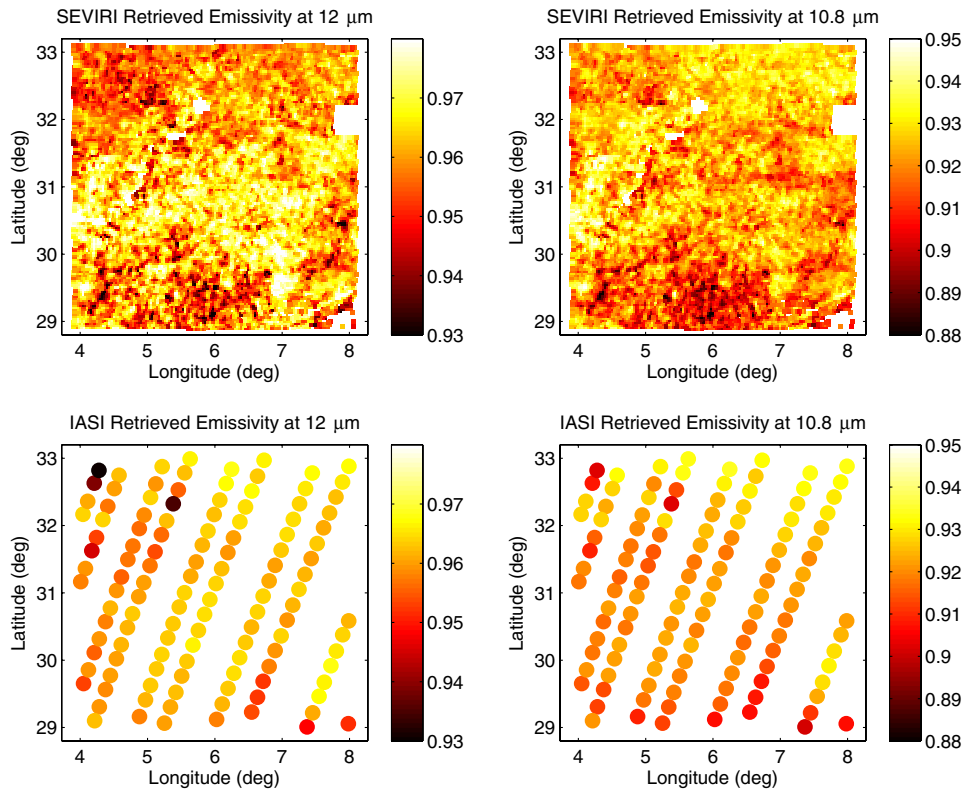

Fig. 18. Same as Fig. 17, but for 1450–2230 cm^{-1}.

Fig. 19. Comparison of SEVIRI (top) and IASI (bottom) emissivity maps for the window channels at 12 and 10.8 μm.

emissivity through convolution of the IASI retrieved emissivity spectrum with the SEVIRI channel spectral response [60].

Figure 19 compares SEVIRI with IASI for the channels at 12 and 10.8 μm. At these channels, desert-sand emissivity has a poor variability, which
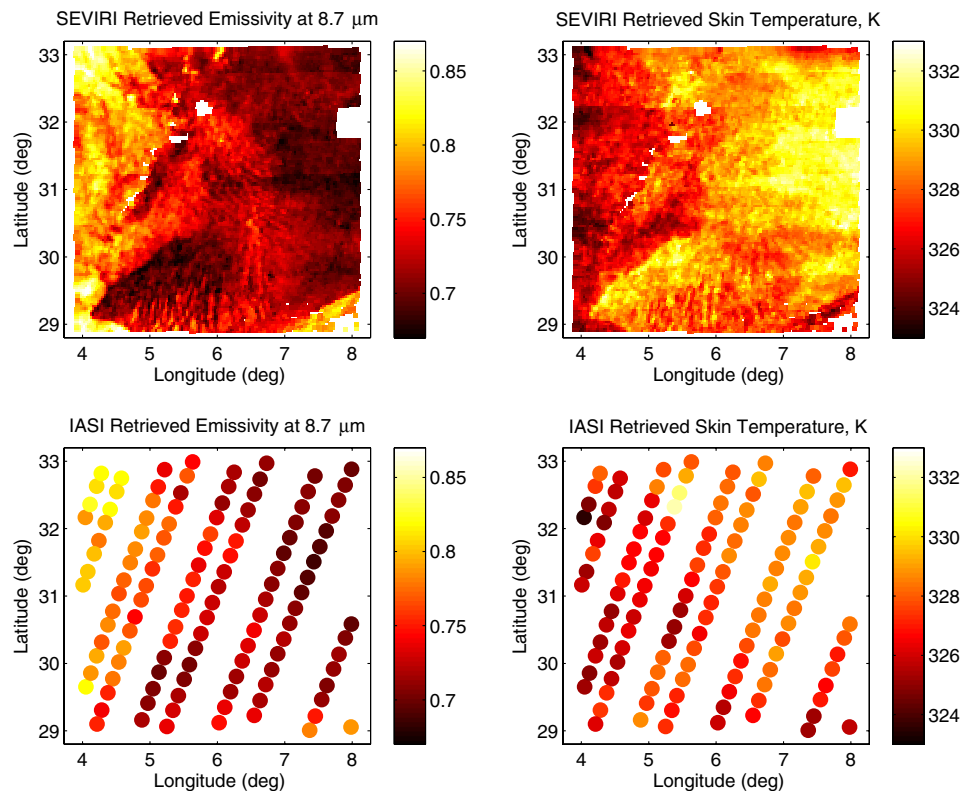

Fig. 20. Comparison of SEVIRI (top) and IASI (bottom) emissivity (channel at 8.7 μm) and skin temperature.

is nicely reflected from the emissivity retrieval. The average difference of emissivity between SEVIRI and IASI (using only the SEVIRI pixels colocated with IASI) is 0.000 at 12 μm and 0.001 at 10.8 μm.

Much more interesting is the comparison at 8.7 μm (shown in Fig. 20), because this channel is located in the middle of the quartz reststrahlen band. Now the emissivity map shows much more variability, and the structures captured by SEVIRI are also nicely seen (although at a coarser spatial resolution) within the IASI map. The average emissivity difference between SEVIRI and IASI is, for this case, −0.004.

Overall, we have that IASI compares very nicely to SEVIRI and that the average values of SEVIRI and IASI emissivity, over the spatial field at hand, differ at the third decimal place alone. A good comparison is also seen for skin temperature (see Fig. 20). Structures seen in the SEVIRI map are also shown in that of IASI and the difference (over the colocated pixels) is ∼0.9 K.

4. Conclusions

We have described and demonstrated the quality and feasibility of a novel approach to derive a high-spectral-resolution emissivity spectrum from IASI observations simultaneously with skin temperature and atmospheric parameters.

The methodology rests on the development in Fourier series of the emissivity spectrum and the formulation of the inverse problem with multiple regularization parameters. We introduce two regularization parameters, one for the atmospheric state vector and one specifically for the emissivity spectrum. Thus, we can deal with the two characteristics of the retrieval problem, atmosphere and surface, separately.

The determination of the two regularization parameters is obtained by the L-hypersurface method [61], which is a direct generalization of the one-parameter L-curve method [30] to the case of two parameters. To the best of our knowledge, the analytical implementation of the scheme described in the paper is completely novel. The methodology has been exemplified with a series of IASI soundings corresponding to passes over regions whose underlying surface has a stable emissivity (desert sand, dune fields, sea surface).

The results show that the methodology is capable of capturing the fine details of the emissivity spectrum and providing a very good fit to the IASI radiance. In fact, the spectral residual is almost zeroed in the atmospheric window.

Although the method makes use of two regularization parameters, which need to be optimized, the procedure is very fast because of its analytical formulation. The methodology can be used to validate low-spectral-resolution surface emissivity extrapolation to the IASI spectral coverage (e.g., [17,62]) and for dedicated science applications, such as the remote sensing from space of composition of mineral and rocks with spectral features in the atmospheric window.

In the present version, we have mostly focused on the presentation and description of the methodology on the basis of few but well-characterized IASI soundings. For applications on a global scale, the system has to be optimized, and a strategy to derive a suitable first guess and background for the emissivity has to be developed. In this respect, we think that the work developed in [17,26,62] could largely simplify the task above and provide a useful framework in which the emissivity first guess and background, in the form needed for IASI, could be developed in such a way to be constrained with laboratory and satellite (MODIS and/or IASI) observations.

Appendix A: Analytical Determination of γ_1 and γ_2 through the L-surface Criterion

It is well known [32] that by introducing the operator $\mathbf{G}$,

$$\mathbf{G} = \mathbf{S}_\epsilon^{-1/2} \mathbf{K} \tilde{\mathbf{S}}_a^{1/2} \qquad (A1)$$

we can write the formal, normalized, solution $\tilde{\mathbf{u}}$ of Eq. (6) according to

$$(\gamma_1 \mathbf{I}_{\gamma_1} + \gamma_2 \mathbf{I}_{\gamma_2} + \mathbf{G}^t \mathbf{G})\hat{\mathbf{u}} = \mathbf{G}^t \tilde{\mathbf{y}}, \qquad (A2)$$

where

$$\hat{\mathbf{u}} = \tilde{\mathbf{S}}_a^{-1/2}(\mathbf{v} - \mathbf{v}_a), \qquad (A3)$$

$$\tilde{\mathbf{y}} = \mathbf{S}_\epsilon^{-1/2}(\mathbf{y} + \mathbf{K}(\mathbf{v}_0 - \mathbf{v}_a)). \qquad (A4)$$

Note that $\mathbf{u}$ is not the same as $\mathbf{x}$ defined in Eq. (6). In fact, $\mathbf{u}$ is the difference of the state vector with respect to the background, whereas in $\mathbf{x}$ the difference against the first guess is considered. In Eq. (A2), $\mathbf{I}_{\gamma_1}$ is a matrix of size $N \times N$ whose elements are zero except for those on the diagonal from row 1 to N_1, which are equal to 1; N_1 is the number of atmospheric parameters in the state vector. Analogously, $\mathbf{I}_{\gamma_2}$ is made by zeros, apart from the diagonal elements (equal to 1) over the rows N_1 to $N_1 + N_2 = N$, with N_2 the number of Fourier coefficients representing the emissivity spectrum.

The determination of the two regularization parameters, γ_1 and γ_2, is obtained by the L-hypersurface method [61], which is a direct generalization of the one-parameter L-curve method [30] to the case of two parameters. Toward this objective, we will develop the 2D L-surface, which, in analogy with the one-dimensional L-curve, is the plot of the residual norm against the size of the two constraints imposed on the solution for all valid regularization parameters. Similar to the L-curve method in which the regularization parameter is selected, which corresponds to the point of the L-curve with maximum curvature, the optimal couple (γ_1, γ_2) is defined to be that corresponding to the point where the L-surface

shows the maximum Gaussian curvature. It is here stressed that the L-surface reduces to the L-curve in the single-parameter case, because the L-surface curvature reduces to the L-curve curvature. The property of the L-hypersurface method has been investigated by Belge et al. [61], who showed that the L-surface pair (γ_1, γ_2) yields a regularized inverse solution, which is numerically equivalent to the optimal solution, in mean-square error. This means that the difference between the two is within the error bars.

The determination of the point of maximum curvature is the key computational issue with the use of the L-surface. Numerical methods are not suited, because the Gaussian curvature may have many secondary local maxima. For this reason, we have resorted to an analytical computation of the Gaussian curvature, which enables us to find the principal maximum.

Taking into account the normalized version of our inverse problem, Eq. (A2), we have the L-surface is defined, in its parametric form, by

$$
L(\gamma_1, \gamma_2) \underset{\text{def}}{=} \begin{cases} \zeta = \Phi(\gamma_1, \gamma_2) = (\mathbf{G\hat{u}} - \tilde{\mathbf{y}})^t (\mathbf{G\hat{u}} - \tilde{\mathbf{y}}) \\ \xi = \Psi(\gamma_1, \gamma_2) = \hat{\mathbf{u}}^t \mathbf{I}_{\gamma_1} \hat{\mathbf{u}} \\ \upsilon = \Omega(\gamma_1, \gamma_2) = \hat{\mathbf{u}}^t \mathbf{I}_{\gamma_2} \hat{\mathbf{u}} \end{cases} . \quad (A5)
$$

The Gaussian curvature is given by [63]

$$
\kappa(\gamma_1, \gamma_2) = \frac{|\det P|}{w^4} \quad (A6)
$$

with

$$
w^2 = 1 + \left(\frac{\partial \zeta}{\partial \xi}\right)^2 + \left(\frac{\partial \zeta}{\partial \upsilon}\right)^2 \quad (A7)
$$

and where $|\det P|$ is the absolute value of the determinant of the matrix $\mathbf{P}$, whose elements are

$$
P_{ij} = \frac{\partial^2 \zeta}{\partial \chi_i \partial \chi_j} \quad (A8)
$$

with $i, j = 1, 2$ and where $\chi_1 = \xi$ and $\chi_2 = \upsilon$. The derivatives above can be obtained by a transformation of the partial derivatives of Φ, Ψ, and Ω with respect to the two regularization parameters, γ_1 and γ_2. Introducing the notation

$$
\begin{cases} \Xi_i = \frac{\partial \Xi}{\partial \gamma_i}, & i = 1, 2, \\ \Xi_{ij} = \frac{\partial^2 \Xi}{\partial \gamma_i \partial \gamma_j}, & i, j = 1, 2, \end{cases} \quad (A9)
$$

to indicate the derivative of a generic function Ξ with respect to γ_1 and γ_2, we have

$$
\begin{cases} \frac{\partial \zeta}{\partial \xi} = g = \frac{\Phi_1}{\Psi_1} + \frac{\Phi_2}{\Psi_2} \\ \frac{\partial \zeta}{\partial \upsilon} = g^* = \frac{\Phi_1}{\Omega_1} + \frac{\Phi_2}{\Omega_2} \end{cases}. \quad (A10)
$$

And for the second derivatives,

$$
\begin{cases} \frac{\partial^2 \zeta}{\partial \xi^2} = \frac{g_1}{\Psi_1} + \frac{g_2}{\Psi_2}; & \frac{\partial^2 \zeta}{\partial \xi \partial \upsilon} = \frac{g_1^*}{\Psi_1} + \frac{g_2^*}{\Psi_2} \\ \frac{\partial^2 \zeta}{\partial \upsilon^2} = \frac{g_1^*}{\Omega_1} + \frac{g_2^*}{\Omega_2}; & \frac{\partial^2 \zeta}{\partial \upsilon \partial \xi} = \frac{g_1}{\Omega_1} + \frac{g_2}{\Omega_2} \end{cases} \quad (A11)
$$

with

$$
\begin{cases} g_1 = \frac{\Phi_{11}}{\Psi_1} - \frac{\Phi_1 \Psi_{11}}{\Psi_1^2} + \frac{\Phi_{12}}{\Psi_2} - \frac{\Phi_2 \Psi_{12}}{\Psi_2^2} \\ g_2 = \frac{\Phi_{22}}{\Psi_2} - \frac{\Phi_2 \Psi_{22}}{\Psi_2^2} + \frac{\Phi_{21}}{\Psi_1} - \frac{\Phi_1 \Psi_{21}}{\Psi_1^2} \\ g_1^* = \frac{\Phi_{11}}{\Omega_1} - \frac{\Phi_1 \Omega_{11}}{\Omega_1^2} + \frac{\Phi_{12}}{\Omega_2} - \frac{\Phi_2 \Omega_{12}}{\Omega_2^2} \\ g_2^* = \frac{\Phi_{22}}{\Omega_2} - \frac{\Phi_2 \Omega_{22}}{\Omega_2^2} + \frac{\Phi_{21}}{\Omega_1} - \frac{\Phi_1 \Omega_{21}}{\Omega_1^2} \end{cases}. \quad (A12)
$$

The notation Ξ_i and Ξ_{ij} for the first and second derivatives allows us to deal with these quantities as though they were elements of a vector and a matrix, respectively. This greatly simplifies the software implementation of an algorithm to compute the Gaussian curvature for each given pair (γ_1, γ_2).

At this point, we need a scheme to compute the derivatives of Φ, Ψ, and Ω. These can be obtained by a direct differentiation of the parametric surface of Eq. (A6). Continuing to use the simplified notation also for the derivatives of the vector solution, $\hat{\mathbf{u}}$, we have for the derivatives of Φ

$$
\begin{cases} \Phi_1 = (\mathbf{G\hat{u}}_1)^t (\mathbf{G\hat{u}} - \tilde{\mathbf{y}}) + (\mathbf{G\hat{u}} - \tilde{\mathbf{y}})^t (\mathbf{G\hat{u}}_1) \\ \Phi_2 = (\mathbf{G\hat{u}}_2)^t (\mathbf{G\hat{u}} - \tilde{\mathbf{y}}) + (\mathbf{G\hat{u}} - \tilde{\mathbf{y}})^t (\mathbf{G\hat{u}}_2) \\ \Phi_{11} = (\mathbf{G\hat{u}}_{11})^t (\mathbf{G\hat{u}} - \tilde{\mathbf{y}}) + 2(\mathbf{G\hat{u}}_1)^t (\mathbf{G\hat{u}}_1) + (\mathbf{G\hat{u}} - \tilde{\mathbf{y}})^t (\mathbf{G\hat{u}}_{11}) \\ \Phi_{22} = (\mathbf{G\hat{u}}_{22})^t (\mathbf{G\hat{u}} - \tilde{\mathbf{y}}) + 2(\mathbf{G\hat{u}}_2)^t (\mathbf{G\hat{u}}_2) + (\mathbf{G\hat{u}} - \tilde{\mathbf{y}})^t (\mathbf{G\hat{u}}_{22}) \\ \Phi_{12} = (\mathbf{G\hat{u}}_{12})^t (\mathbf{G\hat{u}} - \tilde{\mathbf{y}}) + (\mathbf{G\hat{u}}_2)^t (\mathbf{G\hat{u}}_1) + (\mathbf{G\hat{u}}_1)^t (\mathbf{G\hat{u}}_2) + (\mathbf{G\hat{u}} - \tilde{\mathbf{y}})^t (\mathbf{G\hat{u}}_{12}) \\ \Phi_{21} = (\mathbf{G\hat{u}}_{21})^t (\mathbf{G\hat{u}} - \tilde{\mathbf{y}}) + (\mathbf{G\hat{u}}_1)^t (\mathbf{G\hat{u}}_2) + (\mathbf{G\hat{u}}_2)^t (\mathbf{G\hat{u}}_1) + (\mathbf{G\hat{u}} - \tilde{\mathbf{y}})^t (\mathbf{G\hat{u}}_{21}) \end{cases}. \quad (A13)
$$

For the derivatives of Ψ, we have

$$
\begin{cases} \Psi_1 = \hat{\mathbf{u}}_1^t \mathbf{I}_{\gamma_1} \hat{\mathbf{u}} + \hat{\mathbf{u}}^t \mathbf{I}_{\gamma_1} \hat{\mathbf{u}}_1 \\ \Psi_2 = \hat{\mathbf{u}}_2^t \mathbf{I}_{\gamma_1} \hat{\mathbf{u}} + \hat{\mathbf{u}}^t \mathbf{I}_{\gamma_1} \hat{\mathbf{u}}_2 \\ \Psi_{11} = \hat{\mathbf{u}}_{11}^t \mathbf{I}_{\gamma_1} \hat{\mathbf{u}} + 2\hat{\mathbf{u}}_1^t \mathbf{I}_{\gamma_1} \hat{\mathbf{u}}_1 + \hat{\mathbf{u}}^t \mathbf{I}_{\gamma_1} \hat{\mathbf{u}}_{11} \\ \Psi_{22} = \hat{\mathbf{u}}_{22}^t \mathbf{I}_{\gamma_1} \hat{\mathbf{u}} + 2\hat{\mathbf{u}}_2^t \mathbf{I}_{\gamma_1} \hat{\mathbf{u}}_2 + \hat{\mathbf{u}}^t \mathbf{I}_{\gamma_1} \hat{\mathbf{u}}_{22} \\ \Psi_{12} = \hat{\mathbf{u}}_{12}^t \mathbf{I}_{\gamma_1} \hat{\mathbf{u}} + \hat{\mathbf{u}}_2^t \mathbf{I}_{\gamma_1} \hat{\mathbf{u}}_1 + \hat{\mathbf{u}}_1^t \mathbf{I}_{\gamma_1} \hat{\mathbf{u}}_2 + \hat{\mathbf{u}}^t \mathbf{I}_{\gamma_1} \hat{\mathbf{u}}_{12} \\ \Psi_{21} = \hat{\mathbf{u}}_{21}^t \mathbf{I}_{\gamma_1} \hat{\mathbf{u}} + \hat{\mathbf{u}}_1^t \mathbf{I}_{\gamma_1} \hat{\mathbf{u}}_2 + \hat{\mathbf{u}}_2^t \mathbf{I}_{\gamma_1} \hat{\mathbf{u}}_2 + \hat{\mathbf{u}}^t \mathbf{I}_{\gamma_1} \hat{\mathbf{u}}_{21} \end{cases}.
$$

$$
(A14)
$$

Because of the symmetry of two terms Ψ and Ω, the derivatives of Ω are obtained by replacing $\mathbf{I}_{\gamma_1}$ with $\mathbf{I}_{\gamma_2}$ in Eq. (A14).

Finally, it is seen that all the computations above depend on the partial derivatives of the $\hat{\mathbf{u}}$. These can be easily obtained by differentiation of Eq. (A2). We have

$$
\begin{cases}
\mathbf{A}\hat{\mathbf{u}}_1 = -\mathbf{I}_{\gamma_1}\hat{\mathbf{u}} \\
\mathbf{A}\hat{\mathbf{u}}_2 = -\mathbf{I}_{\gamma_2}\hat{\mathbf{u}} \\
\mathbf{A}\hat{\mathbf{u}}_{11} = -2\mathbf{I}_{\gamma_1}\hat{\mathbf{u}}_1 \\
\mathbf{A}\hat{\mathbf{u}}_{22} = -2\mathbf{I}_{\gamma_2}\hat{\mathbf{u}}_2 \\
\mathbf{A}\hat{\mathbf{u}}_{12} = -\mathbf{I}_{\gamma_1}\hat{\mathbf{u}}_2 - \mathbf{I}_{\gamma_2}\hat{\mathbf{u}}_1 \\
\mathbf{A}\hat{\mathbf{u}}_{21} = -\mathbf{I}_{\gamma_2}\hat{\mathbf{u}}_1 - \mathbf{I}_{\gamma_1}\hat{\mathbf{u}}_2
\end{cases}
\tag{A15}
$$

It can be seen that the computation of the Gaussian curvature for each pair (γ_1, γ_2) requires the computation of seven linear systems of equations. However, it also seen that the kernel $\mathbf{A}$ be the same, and therefore, its inversion is required just once for any given pair (γ_1, γ_2). In implementing a software code for the computation of the Gaussian curvature, one has to follow the operations from Eq. (A15) back to Eq. (A6), passing from Eqs. (A14), (A13), (A12), (A11), and (A10), in that order.

To find the maximum of $L(\gamma_1, \gamma_2)$ we consider a 2D grid over the rectangle $[1, 100] \times [1, 100]$. The net is evenly spaced in a (base 10) logarithmic scale, and L is computed at the $n \times n$ grid points

$$
(\gamma_{1i}, \gamma_{2j}) = (10^{2i/(n-1)}, 10^{2j/(n-1)}),
$$
$$
i = 1, \ldots, n; \; j = 1, \ldots, n. \tag{A16}
$$

We normally use $n = 10$.

References

1. J. W. Salisbury and D. M. D'Aria, "Emissivity of terrestrial materials in the 8–14 µm atmospheric window," Remote Sens. Environ. **42**, 83–106 (1992).
2. A. R. Korb, P. Dybwad, W. Wadsworth, and J. W. Salisbury, "Portable Fourier transform infrared spectroradiometer for field measurements of radiance and emissivity," Appl. Opt. **35**, 1679–1692 (1996).
3. S. Clausen, A. Morgenstjerne, and O. Rathmann, "Measurement of surface temperature and emissivity by a multitemperature method for Fourier-transform infrared spectrometers," Appl. Opt. **35**, 5683–5691 (1996).
4. J. A. Sobrino and J. Cuenca, "Angular variation of thermal infrared emissivity for some natural surfaces from experimental measurements," Appl. Opt. **38**, 3931–3936 (1999).
5. K. Yoshimori, S. Tamba, and R. Yokoyama, "Simultaneous measurements of skin sea surface temperature and sea surface emissivity from a single thermal imagery," Appl. Opt. **41**, 4937–4944 (2002).
6. J. Cuenca and J. A. Sobrino, "Experimental measurements for studying angular and spectral variation of thermal infrared emissivity," Appl. Opt. **43**, 4598–4602 (2004).
7. R. O. Knuteson, R. G. Dedecker, W. F. Feltz, B. J. Osbourne, H. E. Revercomb, and D. C. Tobin, "Infrared land surface emissivity in the vicinity of the ARM SGP central facility," presented at the 13th ARM Science Team Meeting, Broomfield, Colorado, 31 March–4 April 2003.
8. R. O. Knuteson, F. A. Best, D. H. DeSlover, B. J. Osborne, H. E. Revercomb, and W. L. Smith, Sr., "Infrared land surface remote sensing using high spectral resolution aircraft observations," Adv. Space Res. **33**, 1114–1119 (2004).
9. W. L. Smith, R. O. Knuteson, H. E. Revercomb, W. Feltz, H. B. Howell, W. P. Menzel, O. Brown, J. Brown, P. Minnett, and W. McKeown, "Observations of the infrared radiative properties of the ocean—implications for the measurement of sea surface temperature via satellite remote sensing," Bull. Am. Meteorol. Soc. **77**, 41–51 (1996).
10. L. Fiedler and S. Bakan, "Interferometric measurements of sea surface temperature and emissivity," Dtsch. Hydrogr. Z. **49**, 357–365 (1997).
11. P. J. Minnett, R. O. Knuteson, F. A. Best, B. J. Osborne, J. A. Hanafin, and O. B. Brown, "The Marine-Atmospheric Emitted Radiance Interferometer: a high-accuracy, seagoing infrared spectroradiometer," J. Atmos. Ocean. Technol. **18**, 994–1013 (2001).
12. S. M. Newman, J. A. Smith, M. D. Glew, S. M. Rogers, and J. P. Taylor, "Temperature and salinity dependence of sea surface emissivity in the thermal infrared," Q. J. R. Meteorol. Soc. **131**, 2539–2557 (2005).
13. G. Masiello, G. Grieco, C. Serio, and V. Cuomo, "Canopy emissivity characterization from hyper spectral infrared observations," presented at the 12th Conference on Atmospheric Radiation, Madison, Wisconsin, 10–14 July 2006, http://ams.confex.com/ams/pdfpapers/112642.pdf.
14. A. Gillespie, S. Rokugawa, T. Matsunaga, J. S. Cothern, S. Hook, and A. B. Kahle, "A temperature and emissivity separation algorithm for Advanced Spaceborne Thermal Emission and Reflection Radiometer (ASTER) images," IEEE Trans. Geosci. Remote Sens. **36**, 1113–1126 (1998).
15. G. Masiello, C. Serio, and V. Cuomo, "Exploiting quartz spectral signature for the detection of cloud-affected satellite infrared observations over African desert areas," Appl. Opt. **43**, 2305–2315 (2004).
16. S. A. Clough, M. W. Shephard, J. Worden, P. D. Brown, H. M. Worden, M. Luo, C. D. Rodgers, C. P. Rinsland, A. Goldman, L. Brown, S. S. Kulawik, A. Eldering, M. Lampel, G. Osterman, R. Beer, K. Bowman, K. E. Cady-Pereira, and E. J. Mlawer, "Forward model and Jacobians for tropospheric emission spectrometer retrievals," IEEE Trans. Geosci. Remote Sens. **44**, 1308–1323 (2006).
17. S. W. Seemann, E. F. Borbas, R. O. Knuteson, G. R. Stephenson, and H.-L. Huang, "Development of a global infrared land surface emissivity database for application to clear sky sounding retrievals from multispectral satellite radiance measurements," J. Appl. Meteorol. Climatol. **47**, 108–123 (2007).
18. Z. Wan, "New refinements and validation of the MODIS land-surface temperature/emissivity products," Remote Sens. Environ. **112**, 59–74 (2008).
19. G. C. Hulley, S. J. Hook, and A. M. Baldridge, "ASTER land surface emissivity database of California and Nevada," Geophys. Res. Lett. **35**, L13401 (2008).
20. E. Péquignot, A. Chédin, and N. A. Scott, "Infrared continental surface emissivity spectra retrieved from AIRS

hyperspectral sensor," J. Appl. Meteorol. Climatol. **47**, 1619–1633 (2008).

21. G. C. Hulley, S. J. Hook, E. Manning, S.-Y. Lee, and E. Fetzer, "Validation of the Atmospheric Infrared Sounder (AIRS) version 5 land surface emissivity product over the Namib and Kalahari deserts," J. Geophys. Res. **114**, D19104 (2009).

22. G. C. Hulley and S. J. Hook, "Intercomparison of versions 4, 4.1 and 5 of the MODIS Land Surface Temperature and Emissivity products and validation with laboratory measurements of sand samples from the Namib desert, Namibia," Remote Sens. Environ. **113**, 1313–1318 (2009).

23. G. C. Hulley and S. J. Hook, "The North American ASTER Land Surface Emissivity database (NAALSED) version 2.0," Remote Sens. Environ. **113**, 1967–1975 (2009).

24. J. Li, J. Li, E. Weisz, and D. K. Zhou, "Physical retrieval of surface emissivity spectrum from hyperspectral infrared radiances," Geophys. Res. Lett. **34**, L16812 (2007).

25. L. Zhou, M. Goldberg, C. Barnet, Z. Cheng, F. Sun, W. Wolf, T. King, X. Liu, H. Sun, and M. Divakarla, "Regression of surface spectral emissivity from hyperspectral instruments," IEEE Trans. Geosci. Remote Sens. **46**, 328–333 (2008).

26. D. K. Zhou, A. M. Larar, X. Liu, W. L. Smith, L. L. Strow, P. Yang, P. Schlüssel, and X. Calbet, "Global land surface emissivity retrieved from satellite ultraspectral IR measurements," IEEE Trans. Geosci. Remote Sens. **49**, 1277–1290 (2011).

27. X. L. Ma, Z. Wan, C. C. Moeller, W. P. Menzel, and L. E. Gumley, "Simultaneous retrieval of atmospheric profiles, land-surface temperature, and surface emissivity from moderate-resolution imaging spectroradiometer thermal infrared data: extension of a two-step physical algorithm," Appl. Opt. **41**, 909–924 (2002).

28. F. Hilton, R. Armante, T. August, C. Barnet, A. Bouchard, C. Camy-Peyret, V. Capelle, L. Clarisse, C. Clerbaux, P.-F. Coheur, A. Collard, C. Crevoisier, G. Dufour, D. Edwards, F. Faijan, N. Fourrié, A. Gambacorta, M. Goldberg, V. Guidard, D. Hurtmans, S. Illingworth, N. Jacquinet-Husson, T. Kerzenmacher, D. Klaes, L. Lavanant, G. Masiello, M. Matricardi, A. McNally, S. Newman, E. Pavelin, S. Payan, E. Péquignot, S. Peyridieu, T. Phulpin, J. Remedios, P. Schlüssel, C. Serio, L. Strow, C. Stubenrauch, J. Taylor, D. Tobin, W. Wolf, and D. Zhou, "Hyperspectral Earth observation from IASI: five years of accomplishments," Bull. Am. Meteorol. Soc. **93**, 347–370 (2012).

29. C. Serio, G. Grieco, G. Masiello, U. Amato, and I. De Feis, "Consolidation of scientific baseline for MTG-IRS level 2 processing: role of OE with background state and associated error from climatology: final report" (EUMETSAT, 2010), available online at http://www2.unibas.it/gmasiello/assite/rep/Delivery%2017_final_report.pdf

30. P. C. Hansen, "Analysis of discrete ill-posed problems by means of the L-curve," SIAM Rev. **34**, 561–580 (1992).

31. C. D. Rodgers, *Inverse Methods for Atmospheric Sounding: Theory and Practice* (World Scientific, 2000).

32. A. Carissimo, I. De Feis, and C. Serio, "The physical retrieval methodology for IASI: the δ-IASI code," Environ. Modell. Software **20**, 1111–1126 (2005).

33. A. Tarantola, *Inverse Problem Theory: Methods for Data Fitting and Model Parameter Estimation* (Elsevier, 1987).

34. U. Amato, G. Masiello, C. Serio, and M. Viggiano, "The σ-IASI code for the calculation of infrared atmospheric radiance and its derivatives," Environ. Modell. Software **17**, 651–667 (2002).

35. R. Siegel and J. R. Howell, *Thermal Radiation Heat Transfer* (McGraw-Hill, 1972).

36. W. M. Elsasser, *Heat Transfer by Infrared Radiation in the Atmosphere* (Harvard University, 1942).

37. K. N. Liou, *Radiation and Cloud Processes in the Atmosphere* (Oxford University, 1992).

38. M. Matricardi, ECMWF, Reading, UK (personal communication, 2012).

39. K. Masuda, T. Takashima, and Y. Takayma, "Emissivity of pure and sea waters for the model sea surface in the infrared

40. R. J. Bell, *Introductory Fourier Transform Spectroscopy* (Academic, 1972).

41. E. A. Robinson and M. T. Silvia, *Digital Foundation of Time Series Analysis: Wave-Equation Space-Time Processing*, Vol. **2** (Holden-Day, 1981).

42. W. C. Snyder and Z. Wan, "BRDF models to predict spectral reflectance and emissivity in the thermal infrared," IEEE Trans. Geosci. Remote Sens. **36**, 214–225 (1998).

43. A. M. Baldridge, S. J. Hook, C. I. Grove, and G. Rivera, "The ASTER spectral library version 2.0," Remote Sens. Environ. **113**, 711–715 (2009).

44. G. Masiello, C. Serio, and P. Antonelli, "Inversion for atmospheric thermodynamical parameters of IASI data in the principal components space," Q. J. R. Meteorol. Soc. **138**, 103–117 (2012).

45. U. Amato, V. Cuomo, I. De Feis, F. Romano, C. Serio, and H. Kobayashi, "Inverting for geophysical parameters from IMG radiances," IEEE Trans. Geosci. Remote Sens. **37**, 1620–1632 (1999).

46. A. M. Lubrano, C. Serio, S. A. Clough, and H. Kobayashi, "Simultaneous inversion for temperature and water vapor from IMG radiances," Geophys. Res. Lett. **27**, 2533–2536 (2000).

47. G. Masiello, C. Serio, and H. Shimoda, "Qualifying IMG tropical spectra for clear sky," J. Quant. Spectrosc. Radiat. Transfer **77**, 131–148 (2003).

48. U. Amato, A. Antoniadis, I. De Feis, G. Masiello, M. Matricardi, and C. Serio, "Technical note: Functional sliced inverse regression to infer temperature, water vapour and ozone from IASI data," Atmos. Chem. Phys. **9**, 5321–5330 (2009).

49. G. Masiello, C. Serio, A. Carissimo, G. Grieco, and M. Matricardi, "Application of φ-IASI to IASI: retrieval products evaluation and radiative transfer consistency," Atmos. Chem. Phys. **9**, 8771–8783 (2009).

50. G. Grieco, G. Masiello, and C. Serio, "Interferometric vs spectral IASI radiances: effective data-reduction approaches for the satellite sounding of atmospheric thermodynamical parameters," Remote Sens. **2**, 2323–2346 (2010).

51. G. Masiello, M. Matricardi, and C. Serio, "The use of IASI data to identify systematic errors in the ECMWF forecasts of temperature in the upper stratosphere," Atmos. Chem. Phys. **11**, 1009–1021 (2011).

52. G. Masiello, M. Amoroso, P. Di Girolamo, C. Serio, S. Venafra, and T. Deleporte, "IASI Retrieval of temperature, water vapor and ozone profiles over land with φ-IASI package during the COPS campaign," in *Proceedings of the 9th International Symposium on Tropospheric Profiling* (ESA, 2012), http://cetemps.aquila.infn.it/istp/proceedings/Session_I_Water_vapor_ozone_and_trace_gases/SI_02_Masiello.pdf.

53. V. Wulfmeyer, A. Behrendt, H.-S. Bauer, C. Kottmeier, U. Corsmeier, A. Blyth, G. Craig, U. Schumann, M. Hagen, S. Crewell, P. Di Girolamo, C. Flamant, M. Miller, A. Montani, S. Mobbs, E. Richard, M. W. Rotach, M. Arpagaus, H. Russchenberg, P. Schlüssel, M. König, V. Gärtner, R. Steinacker, M. Dorninger, D. D. Turner, T. Weckwerth, A. Hense, and C. Simmer, "The Convective and Orographically Induced Precipitation Study: a research and development project of the World Weather Research Program for improving quantitative precipitation forecasting in low-mountain regions," Bull. Am. Meteorol. Soc. **89**, 1477–1486 (2008).

54. J. P. Taylor, "Facility for Airborne Atmospheric Measurements (FAAM): Joint Airborne IASI (Infrared Atmospheric Sounding Interferometer) Validation Experiment (JAIVEX) measurements," http://badc.nerc.ac.uk/data/jaivex/.

55. N. Lancaster, "Grain size characteristics of Namib Desert linear dunes," Sedimentology **28**, 115–122 (1981).

56. K. White, J. Walden, and S. D. Gurney, "Spectral properties, iron oxide content and provenance of Namib dune sands," Geomorphology **86**, 219–229 (2007).

57. E. D. McKee, ed., "A study of global sand seas: Ancient sandstones considered to be Eolian," *US Geological Survey Professional Paper Nr. 1052* (US Geological Survey, 1979).

58. G. Masiello, C. Serio, F. Esposito, and L. Palchetti, "Validation of line and continuum spectroscopic parameters with measurements of atmospheric emitted spectral radiance from far to mid infrared wave number range," J. Quant. Spectrosc. Radiat. Transfer **113**, 1286–1299 (2012).

59. V. G. Tyuterev, A. M. Perrin, and L. S. Rothman, eds., "Three leaders in spectroscopy," (Special Issue), J. Quant. Spectrosc. Radiat. Transfer **113**, 821–1406 (2012).

60. I. De Feis, G. Masiello, C. Serio, M. Amoroso, and S. Venafra, "Spatio-temporal constraints for emissivity and surface temperature retrieval: preliminary results and comparisons for SEVIRI and IASI observations," presented at the 3rd IASI International Conference, Hyères, France, 4–8 February 2013, available online at http://www.iasi2013.com/oral/08_03-De_Feis_Italia.pdf.

61. M. Belge, M. E. Kilmer, and E. L. Miller, "Efficient determination of multiple regularization parameters in a generalized L-curve framework," Inverse Probl. **18**, 1161–1183 (2002).

62. E. E. Borbas and B. C. Ruston, "The RTTOV UWiremis IR land surface emissivity module," Doc. NWPSAF-MO-VS-042 (EUMETSAT, 2010).

63. H. Flanders, *Differential Forms with Applications to the Physical Sciences* (Dover, 1989).